Elevated *in-situ* Vp/Vs preceding hydraulic-fracturing-induced earthquakes

Jian Xu[1,2*], Yajing Liu[1*], Junlun Li[2,4,5*], Marco P. Roth[3], Rebecca M. Harrington[3], Yicheng He[6]

[1]Department of Earth and Planetary Sciences, McGill University, Montreal, Quebec, Canada.
[2]State Key Laboratory of Precision Geodesy, School of Earth and Space Sciences, University of Science and Technology of China, Hefei 230026, China.
[3]Institute of Geosciences, Ruhr University Bochum, Bochum, Germany.
[4]Mengcheng National Geophysical Observatory, University of Science and Technology of China, Hefei, Anhui, China.
[5]Anhui Provincial Key Laboratory of Subsurface Exploration and Earthquake Hazard Prevention, Hefei, 230031, China
[6]Jiangsu Earthquake Agency, Nanjing, China.

Corresponding authors: Jian Xu (jian.xu2@mail.mcgill.ca)

Yajing Liu (yajing.liu@mcgill.ca)

Junlun Li (lijunlun@ustc.edu.cn)

This manuscript is a non-peer-reviewed preprint submitted to EarthArXiv.

Abstract

Effective management of seismic hazard in geo-energy development demands real-time estimates of subsurface fault instability. However, real-time monitoring of pore pressure change during subsurface fluid injection remains challenging. Here, we present a novel high-resolution, non-tomographic monitoring strategy that tracks the ratio of seismic wave speeds (Vp/Vs) as a proxy for pore pressure coevolution with induced seismicity clusters. Applying this strategy to the southern Sichuan Basin, China, we observe distinct elevated *in-situ* Vp/Vs ratios that precede the occurrence of M>3 hydraulic-fracturing (HF) induced earthquakes by an intervening period of several days of seismic quiescence. This quiescent period reveals a prolonged nucleation phase, during which injected fluids gradually condition the M3–M4 rupture zones by elevating pore pressure to critical levels. Such a prolonged nucleation phase could provide a valuable time window for operational intervention, offering more precise timing for hazard mitigation than traditional magnitude-based traffic-light protocols. Our results suggest a viable strategy for near-real-time seismic hazard assessment in diverse fluid-rich environments susceptible to either induced or natural earthquakes.

Introduction

Fluid-injection-induced seismicity has garnered growing global attention[1–4]. The recorded maximum magnitudes of fluid-injection-induced earthquakes exhibit an upward trend worldwide and reach up to M6.0, as reported in the southern Sichuan basin, China[5,6]. These moderate-to-strong ($3 \leq M \leq 6$) induced earthquakes have caused considerable nuisance, damage and even casualties[4,6,7]. Three end-member mechanisms associated with fluid injection are commonly invoked to explain the earthquake triggering process: pore pressure increase[8,9], poroelastic stress perturbation[10,11], and aseismic slip[12,13]. Elevated pore pressure is considered the dominant triggering mechanism, as indicated by extensive field observations of the spatiotemporal distribution of induced seismicity[14–16]. Thus, how to track subsurface

pore-pressure evolution is critical for both understanding the earthquake nucleation process and designing seismic hazard mitigation strategies.

Two observational approaches are commonly used to infer elevated pore pressure: 1) tracking the migration of seismicity[8,17,18], and 2) resolving tomographic velocity (ratio) anomalies[19,20]. However, the seismicity migration pattern itself provides little to no constraints on the pore pressure levels required for fault slip assessment[21]. On the other hand, travel-time-based tomographic approaches typically lack temporal resolution and can only resolve velocity heterogeneities on the order of several kilometers, or larger[5,19,22]. These limitations on resolution render both methods unsuitable for resolving the fault slip tendency or nucleation processes of moderate-to-strong induced earthquakes in real time during fluid injection. While the recently proposed time-lapse dv/v imaging techniques using seismic ambient noise can achieve time resolution on the order of months to days[23,24], they still suffer from intrinsic trade-offs between spatial resolution and depth sensitivity inherent to surface wave inversion. To our knowledge, real-time pore pressure monitoring with sub-kilometer resolution in the source regions of induced earthquakes has not been achieved.

In this work, we present a non-tomographic approach that measures spatiotemporal variations of *in-situ* Vp/Vs to monitor the near-source pore pressure evolution at/near seismogenic faults[25]. The spatiotemporal resolution of this method relies primarily on the number of phase arrivals and the spatial compactness of seismicity, which are limiting factors in previous applications to obtain robust solutions at both sub-day and sub-kilometer scales[26,27]. With abundant clustered-induced seismicity and dense seismic arrays, the Changning shale gas field (CSF) in the southern Sichuan basin offers a natural testbed for monitoring the spatiotemporal variations of *in-situ* Vp/Vs at high resolution.

In the CSF, over 550 HF wells have been completed since 2011. Owing to high differential stresses[28], pervasive seismogenic faults[29], and slip-weakening rock frictional behavior[30], more than 100,000 earthquakes with a magnitude of completeness $M_c = 0.7$ have been cataloged in association with high pore-pressure fluid injection. Over the past decade, the CSF has experienced 3 $M \geq 5$ events, 28 $M \geq 4$ events

and over 200 $M \geq 3$ events[5], ranking it one of the most severe induced-seismicity hazard regions worldwide. To investigate the nucleation process of moderate earthquakes driven by injected fluids, we focus on two M>3 seismic clusters in the CSF that are well covered by dense seismic arrays with publicly available HF injection schedules (Fig. 1). We adapt the *in-situ* Vp/Vs technique to these two clusters using enhanced seismicity catalogues developed by Xu et al.[31] and Ye et al.[32]. The resulting high-resolution *in-situ* Vp/Vs variations distinctly illuminate near-source pore pressure evolution and nucleation processes of the M>3 events. The results demonstrate that *in-situ* Vp/Vs tracking with a dense seismic network can be used as a reliable strategy for real-time seismic hazard assessment.

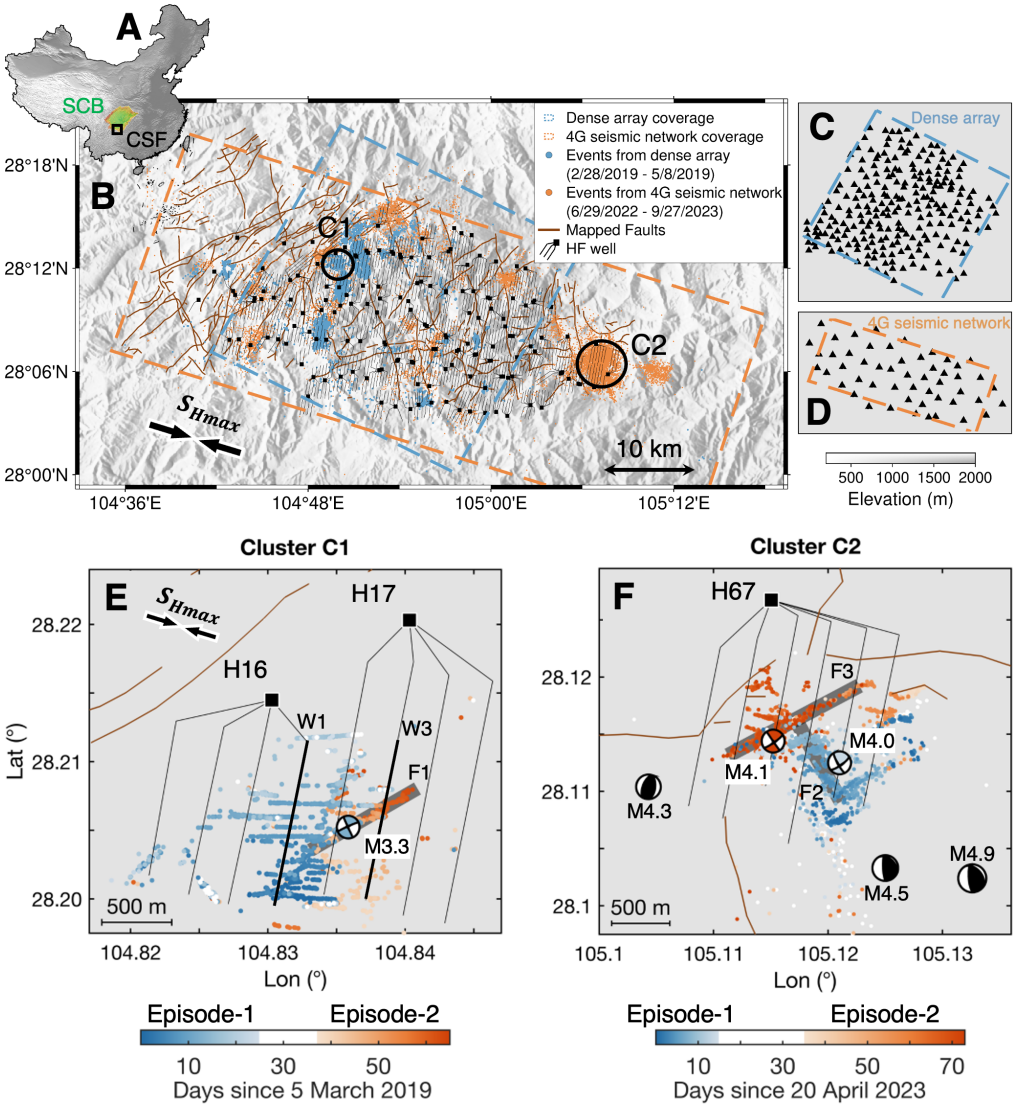

Fig. 1. Changning shale gas field (CSF) with seismicity recorded by two dense seismic arrays. (**A**) CSF in the southern Sichuan Basin (SCB), southwest China. (**B**)

Distribution of hydraulic fracturing well pads (black squares), horizontal well trajectories (black lines) and mapped fault traces (dark red lines) in the production Wufeng-Longmaxi formation[29]. Dashed blue and orange boxes indicate areas covered by dense seismic array and 4G seismic network with station distribution detailed in (C) and (D). Blue and orange dots denote seismicity detected by the dense array and the 4G seismic network, respectively. Two black circles highlight clusters C1 and C2. The arrows at the bottom lower left indicate the local maximum horizontal stress (S_{Hmax}) oriented at $N107^{\circ}$[5]. (**C**) Station distribution of the dense seismic array deployed between 28 February 2019 and 8 May 2019. (**D**) Station distribution of the 4G seismic network deployed since July 2022. (**E**) Spatiotemporal evolution of cluster C1. The earthquake dots are color-coded by time, with the M3.3 mainshock highlighted by a beachball. "Episode-1" and "Episode-2" denote two respective injection periods of wells W1 in pad H16 and W3 in pad H17, with an interval without injection (white interval). Gray band highlights Fault F1. (**F**) Spatiotemporal evolution of cluster C2. Beachballs denote five $M \geq 4$ events: colored beachballs indicate the mainshocks that occurred during hydraulic fracturing, and black beachballs indicate the mainshocks that occurred in the suspension period. Gray bands highlight two distinct faults (F2 and F3) hosting the M4.0 and M4.1 events.

Results

Seismic clusters and HF injection activity

We focus on two seismic clusters (C1 and C2) that occurred during fluid injection in nearby HF wells (Fig. 1). Cluster C1 is derived from an enhanced catalogue developed by Xu et al.[31] using a 336-station dense nodal array with an average interstation spacing of 1.5 km (Figs. 1C, 1E). This cluster lasted for about two months from 5 March to 8 May 2019, with magnitudes ranging from $M_L-1.7$ to $M_L3.3$ (Supplementary Fig. 1). Cluster C2 was monitored by a local seismic network consisting of 48 stations with 4G real-time telemetry (Figs. 1D, 1F)[32]. Events in C2 occurred during an ~80-day period from 20 April to 10 July 2023, with magnitudes ranging from M_L0 to $M_L4.9$. Both clusters exhibit similar spatial-temporal-magnitude evolution, characterized by initial low-magnitude (M<3) seismicity on fractures stimulated by successive HF stages, followed by interaction with pre-existing faults that lead to moderate M3–M4 events. The pre-existing faults F1–F3 are delineated by

integrating microseismicity lineations and focal mechanism solutions of moderate earthquakes (Figs. 1E, 1F).

Cluster C1 spans a horizontal length of ~1.5 km and concentrates at a depth of ~1 km below the HF interval (Fig. 1E). It consists of two nearby seismicity episodes triggered by stimulation along HF wells H16-W1 and H17-W3, respectively. Both episodes exhibit a northward migration pattern following the fluid injection footprints (Supplementary Movie 1). The migration process delineates an initial activation of multiple E-W-striking fractures nearly perpendicular to the HF well trajectories, followed by reactivation of a NEE-trending fault F1 that hosts the largest event (M3.3) of this sequence. HF treatment was not suspended after the M3.3 event, and seismicity in Episode-1 continued to migrate northward until completion of well H16-W1. Injection in the adjacent well H17-W3 commenced 13 days later, triggering the second episode of seismicity which extended further northeast along F1, but without producing any M>3 events.

Cluster C2 also comprises two episodes of seismicity concentrated at ~800 m below the horizontal wells (Fig. 1F). It delineates a set of NEE- and NNW-striking conjugate faults that were sequentially reactivated from southeast to northwest (Supplementary Movie 2). During the first episode, an M4.0 strike-slip event occurred along an NNW-trending fault (F2) after approximately 13 days of seismic activity. The M4.0 event exceeded the red-light threshold of the local traffic-light protocol, leading to an immediate suspension of injection. Three larger earthquakes (M4.5, M4.9 and M4.3) successively occurred over the following three days after the suspension. These events are located outside the well trajectories and have hypocentral depths that are either ~1 km below, or shallower than the first episode of seismicity (Supplementary Fig. 2). We exclude these peripheral events in the following analysis, since they are likely cascading effects from Episode-1 seismicity and are less directly related to pore pressure change during the HF operation. HF operation resumed after ~20 days of suspension, and triggered Episode-2 seismicity along a NEE-trending fault (F3) conjugate to F2. Following 10 days of persistent seismicity, an M4.1 strike-slip event

eventually occurred on fault F3. Further details about these two seismicity catalogues can be found in Methods.

Time-lapse in-situ Vp/Vs

The *in-situ* Vp/Vs technique estimates the near-source Vp/Vs by fitting differential P- and S-wave travel times from clustered events (Methods)[25]. With dense seismic arrays and abundant clustered seismicity, we improve the resolution of the traditional *in-situ* Vp/Vs method by introducing a spatiotemporal moving window for each event. In cluster C1, we apply a spatiotemporal window of 150 m and 2 days to ensure at least 30 nearby events and typically more than 1000 differential travel-time data points are included for each Vp/Vs estimate (Methods). The 150-m spatial window is selected as three times the averaged event location error of 50 m. Cluster C2 was recorded by relatively fewer stations, resulting in larger location errors of 70 m. We adopt a longer time window of 3 days and a larger radius of 200 m. For both clusters, we only retain the Vp/Vs results with Root-Mean-Square Error (RMSE) less than 0.02 and theoretical bias smaller than 0.01 (Methods). We thus regard each Vp/Vs ratio as an *in-situ* property at the hypocenter and origin time of the event centered at the spatiotemporal window. This definition allows each event to be associated with a corresponding Vp/Vs value. The resolution of the Vp/Vs variation in this study reaches up to ~150 m (i.e., the window size), comparable to the source length of M2-M3 earthquakes, so that we can further interpret the Vp/Vs evolution in the context of the nucleation processes of moderate earthquakes.

For cluster C1, we observe stable Vp/Vs ratios around 1.73 for the seismicity on the E-W oriented fractures, except for a 300-m-long patch of elevated Vp/Vs (~1.8) near the prospective M3.3 hypocenter on the NEE-trending fault F1 (Fig. 2A). This high Vp/Vs anomaly emerged 7 days before the M3.3 mainshock (Fig. 2C) and occurred at the intersection of the hydraulic fractures and the seismogenic fault F1. We also observe that events associated with high Vp/Vs values gradually migrated northeast along fault F1 toward the eventual M3.3 hypocenter (Fig. 2C). The M3.3 mainshock itself cannot be assigned a Vp/Vs value because there are no foreshocks on

F1 within a two-day window. After 35 days following the M3.3 event, the second seismicity episode exhibited a recurrence of high Vp/Vs patches that continued to extend northeastward along F1.

In cluster C2, the source regions of both the M4.0 and M4.1 events also exhibit a high Vp/Vs ratio greater than 1.8 (Fig. 2B). Elevated Vp/Vs values are observed ~10 days before the M4.0 event on fault F2 (Fig. 2D). Similar to the M3.3 event, paucity of foreshocks in a 3-day window precludes Vp/Vs estimation for the M4.0 mainshock. The apparent lateral offset between the M4.0 epicenter and the high Vp/Vs patch along F2 arises from the ~200 m shallower depth of the M4.0 event on the southwest-dipping fault F2. The Vp/Vs values in the M4.1 source region show an increasing trend starting from 10 days before the mainshock, during which the seismicity migrated toward the mainshock hypocenter (Fig. 2D).

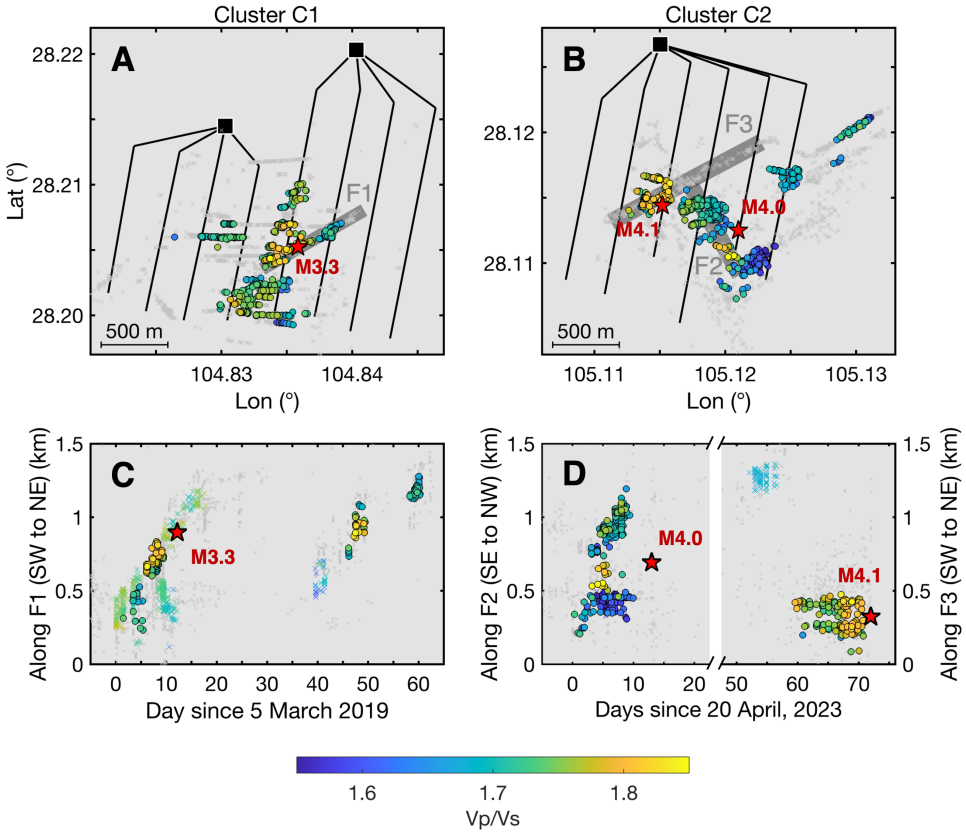

Fig. 2. Spatiotemporal evolution of in-situ Vp/Vs. (**A**) Spatial distribution of Vp/Vs for cluster C1. Dots represent earthquakes color-coded by the Vp/Vs values. Gray crosses indicate seismicity without stable Vp/Vs results. Red star highlights the M3.3 mainshock. Gray band represents fault F1. (**B**) Same as in (A) for cluster C2. Gray bands represent faults F2 and F3. (**C**) Temporal Vp/Vs evolution in cluster C1 projected

along F1. Colored circles and crosses denote Vp/Vs values for events located within and beyond 150 m of perpendicular distance to F1, where 150 m corresponds to the radius used for each Vp/Vs calculation. (**D**) Same as (C), showing the M4.0 sequence (days before 20) and the M4.1 sequence (days after 50) in cluster C2, projected along faults F2 and F3, respectively. The distance threshold for discriminating events within and beyond the fault zone is 200 m for F2 and F3.

Multi-stage evolution of mainshock sequences

The spatiotemporal variation of *in-situ* Vp/Vs characterizes a four-stage evolution of the M3.3 sequence in cluster C1 (Figs. 3A, 3B). In the first stage (S1), several E–W-oriented fractures progressively grew to the south of F1 during HF operations and generated earthquakes with relatively moderate Vp/Vs of around 1.73. From 7 to 2 days prior to the M3.3 event in the second stage (S2), elevated Vp/Vs values emerged as seismicity migrated from HF well-perpendicular fractures onto fault F1. In this stage, multiple fractures intersected the fault and repeatedly elevated Vp/Vs values (>1.8) prior to the mainshock. Following the elevated Vp/Vs, however, the seismicity rate on F1 dropped substantially, resulting in a ~2-day period of quiescence (S3) preceding the M3.3 mainshock. We regard the stages of S2 and S3 as the nucleation phase of the M3.3 main event, which will be discussed in detail below. In the final stage (S4), the aftershock rate on F1 remained low despite continuing HF operations.

A similar multi-stage evolution of initial elevated Vp/Vs followed by foreshock quiescence and then a paucity of aftershocks is also observed for the M4.0 event in cluster C2 (Figs. 3C, 3D). Elevated Vp/Vs values for earthquakes within 200 m of fault F2 appeared about 10 days before the M4.0 mainshock, followed by ~4 days of foreshock quiescence before the mainshock. Sparse aftershocks were observed within 200 m of F2 similar to those of the M3.3 event.

In contrast, the M4.1 event was preceded by persistent foreshock activity without an intervening quiescent stage S3 (Figs. 3E, 3F). Foreshocks of the M4.1 event initiated on multiple fractures perpendicular to the well trajectory and subsequently migrated onto the nearby NEE-trending fault F3 during stages S1 and S2. The Vp/Vs values increased from ~1.75 to 1.8–1.85 starting from 10 days prior to the mainshock. We

cannot evaluate the aftershock pattern of the M4.1 event due to data loss between July 2 and July 8, 2023.

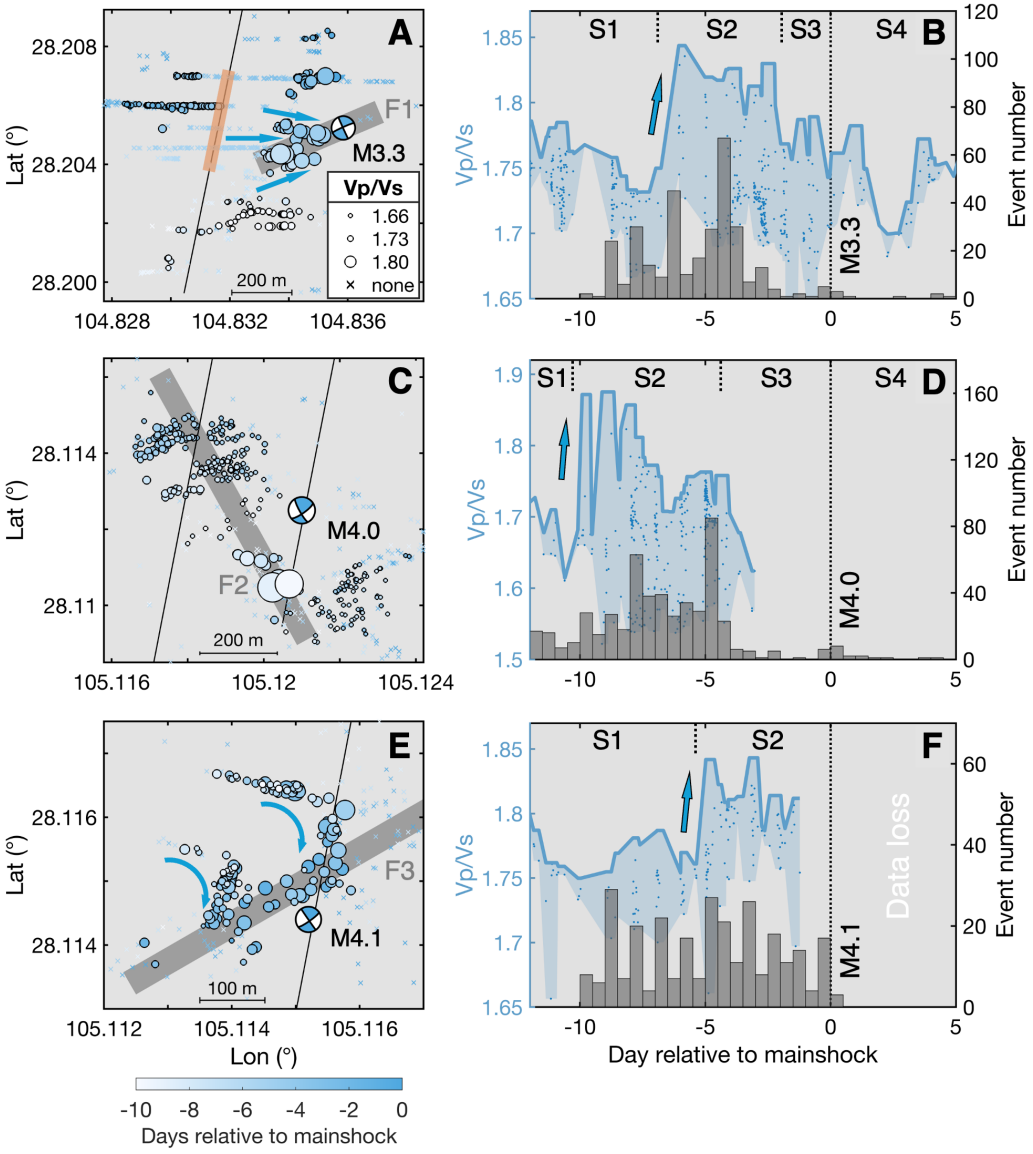

Fig. 3. Nucleation process for three mainshocks. (**A**) Seismicity and Vp/Vs evolution in the 10 days prior to the M3.3 event. Circles and crosses indicate earthquakes with or without stable Vp/Vs estimates, respectively. Circle size is proportional to Vp/Vs value. Colors denote earthquake origin time with respect to the mainshock. Gray band highlights fault F1. Black line denotes well trajectory of H16-W1, and orange band highlights the well segment that underwent a large daily injection volume higher than 4000 m^3. Blue arrows indicate the migration of seismicity from fractures to fault. (**B**) Temporal evolution of Vp/Vs ratios. Histograms denote seismicity rate in 0.5-day bins within 150 m of F1. Blue dots represent all the events with Vp/Vs values shown in (A), and blue line shows the maximum Vp/Vs, computed using a 0.5-day moving window. Blue arrow highlights elevated Vp/Vs values in Stage 2. (**C, D**) The same as (A, B), but for the M4.0 mainshock in cluster C2. (**E, F**) The same as (C, D), but for the M4.1

mainshock. Histograms in (D, F) denote seismicity rate of events within 200 m of F2 and F3.

Discussion

Spatiotemporal variations of Vp/Vs can be attributed to inherently heterogeneous lithology, temporal variation in fluid content, or a combination of both[33–35]. In our study, the spatial distribution of Vp/Vs ratios exhibits no apparent correlation with the reflection amplitudes on the co-located active-source seismic reflection profiles (Supplementary Fig. 3), suggesting that the Vp/Vs variations are not primarily controlled by local lithologic structures. A temporal increase of average Vp/Vs values from ~1.73 to ~1.8 is observed in the source region of the M4.1 foreshock sequence (Fig. 4A), further indicating a time-dependent, non-lithologic controlling factor. The spatiotemporal variation of Vp/Vs, in particular the increase leading up to the M3–M4 events, more likely reflects progressive fluid accumulation as injected fluids diffuse from hydraulic fractures onto pre-existing faults. Below, we estimate the porosity and pore pressure increases accountable for the observed elevated *in-situ* Vp/Vs, and assess their implications for the nucleation of the three M>3 mainshocks, as well as the accompanying quiescence of foreshocks and aftershocks.

Estimates of Porosity and pore pressure changes

Porosity changes are widely invoked to account for seismic velocity anomalies for both tectonic and induced earthquakes[27,36,37]. We calculate the variation of Vp/Vs ratio with porosity and crack aspect ratio based on two approaches, the Kuster-Toksöz theory[38] and the self-consistent method[39]. The theoretical calculations suggest that a monotonic increase in Vp/Vs with porosity is obtained only for crack aspect ratios smaller than 0.03 (Fig. 4B; Methods). Such small aspect ratios have been well documented in fault damage zones[40,41]. An increase in Vp/Vs from ~1.73 to ~1.80 requires approximately 1.3% and 8.6% increases in porosity for crack aspect ratios of 0.01 and 0.03, respectively. By comparison, the inferred high porosity in the earthquake source region is similar to the 1.5–8% porosity estimated across the fluid-rich segment

of the Gofar transform fault that hosts abundant seismic swarms and foreshocks to M5+ earthquakes[42,43].

While porosity increase may explain the observed elevated Vp/Vs values, they cannot provide a direct quantitative measure of fault slip tendency or potential seismic hazard. Thus, we explore pore pressure changes as an alternative explanation and assess their impact on Vp/Vs. We estimate pore pressure changes using an experimental effective-stress framework in which elastic wave velocities are measured under different pore pressure and confining stress conditions[44,45]. As for the M4.1 event, the ~4% increase in Vp/Vs from 1.73 to 1.80 prior to the mainshock corresponds to a pore pressure increase of ~13–19 MPa in sedimentary rocks such as dolomite (Fig. 4C; Methods), a lithology consistent with that of the seismogenic formation for moderate induced earthquakes in the CSF[5,31]. These estimates are consistent with the overpressure of up to ~15–25 MPa inferred from stress regime inversion using focal mechanisms in the CSF[20].

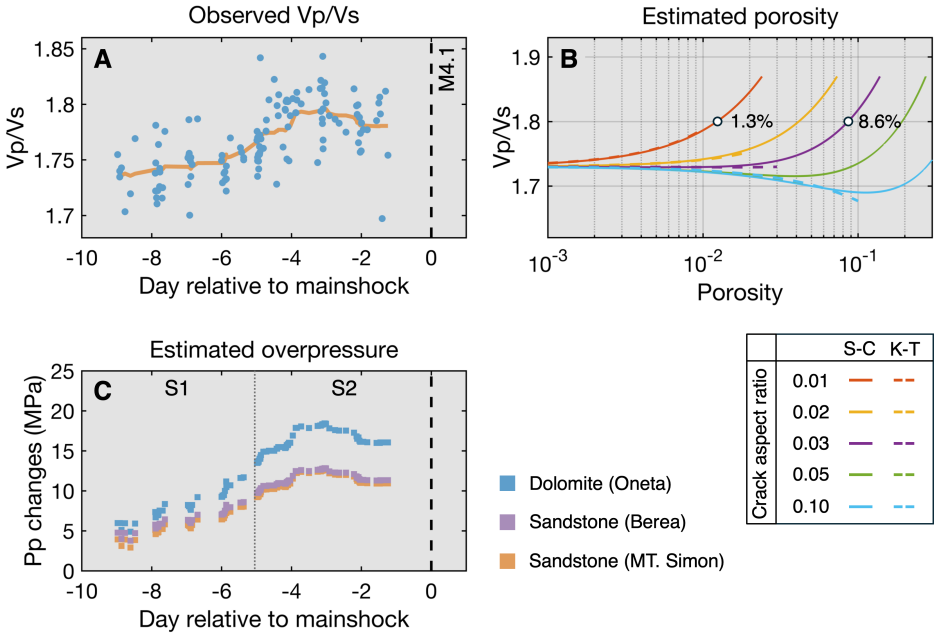

Fig. 4. Porosity and pore pressure estimates for the M4.1 event. (**A**) In-situ Vp/Vs ratios during the foreshocks of the M4.1 event (Fig. 3E), with its origin time marked by the black dashed line. Orange line shows the mean Vp/Vs values calculated by a 2-day moving window. (**B**) Theoretical calculation of Vp/Vs with different assumptions of porosities and crack aspect ratios using both Kuster-Toksöz crack theory (K-T) [38] and a self-consistent method (S-C) [39]. (**C**) Pore pressure changes estimated by the mean

Vp/Vs values in (A), using the velocity-pore pressure relation measured in different rock samples (Methods). S1 and S2 indicate two stages defined in Fig. 3F.

Nucleation processes of M>3 mainshocks

The seismicity in clusters C1 and C2 migrates along multiple fluid diffusion fronts with diffusivity values ranging from ~0.005 and ~0.1 m^2/s (Fig. 5A; Methods), suggesting a complex hydraulic system. The fluid diffusion and accumulation coeval with the increasing Vp/Vs from adjacent fractures to the eventual seismogenic faults may control the nucleation processes of these mainshocks. The fractures and faults in our study area likely contain asperities of varying sizes, friction coefficients, permeabilities and heterogeneous stress states[46,47]. When primed by fluid diffusion and elevated pore pressure, these asperities may rupture in earthquakes of different magnitudes. For the M4.1 sequence in cluster C2, *in-situ* Vp/Vs changes imply a moderate pore pressure increase of 5–10 MPa at stage S1 when fluids diffuse along fractures (Fig. 4C). At this stage, relatively smaller asperities are preferentially reactivated to generate smaller M<3 events. Then, continuous fluid injection progressively reactivates proximal fractures as permeable pathways and eventually establish hydraulic connections between the treatment wells and pre-existing faults. Fluids gradually accumulate onto the fault zone (F3) at stage S2 and increase the pore pressure by over 10 MPa, eventually initiating the nucleation of the M4.1 on a larger asperity with a greater unclamping effect.

The nucleation process of the M3.3 event is similar to that of the M4.1 event with a more pronounced stage S2 of fluid diffusion along the fault toward the M3.3 hypocenter (Fig. 3A). The migrating seismicity with elevated Vp/Vs values are correlated spatiotemporally with the large daily injection volumes 2–5 days before the mainshock (orange band in Fig. 3A and Supplementary Fig. 4), suggesting that these high injection volumes likely act as the driver for pore pressure buildup. The inference of injection-driven fluid accumulation aligns well with McGarr[48], in that larger injection volumes could promote larger induced earthquakes by generating higher pore pressure on preexisting faults. High pore pressure conditions can also be inferred from the second episode of high Vp/Vs, when fluid injection resumed along well H17-W3

approximately 35 days after the M3.3 event (Fig. 2C). However, no M>3 events occurred during the second episode, suggesting that the background shear stress was either fully or partially released by the previous M3.3 event, which is also supported by the lack of aftershocks (Fig. 3B). As a result, preparing the fault for another M3 failure would likely take significantly more time.

The M3.3 and M4.0 earthquake sequences exhibit an additional stage S3 of foreshock quiescence prior to the mainshocks (Figs. 3B and 3D), which we interpret in the next subsection as a prolonged nucleation phase that may expand the subsequent main rupture areas.

Prolonged nucleation phase during foreshock quiescence

The foreshock quiescent period can be regarded as a prolonged nucleation phase, during which diffusing pore pressure conditions a broader fault area for imminent rupture of a larger mainshock. Rupture areas of larger events would be expected to have higher pre-rupture strength that requires a greater amount of stress accumulation or significant strength weakening prior to failure[49–51]. The observed foreshock quiescence may reflect the process of fluid diffusion into such strong fault patches that small events are unlikely to be triggered until pore pressure accumulates sufficiently.

For the M3.3 and M4.0 earthquake sequences, foreshock migration along faults F1 and F2 can be well characterized by diffusivity values of 0.025 m^2/s and 0.075 m^2/s, respectively (Fig. 5B). In both sequences, the foreshocks associated with elevated Vp/Vs>1.8 consistently follow a lower diffusivity value of 0.025 m^2/s, indicating relatively lower permeability favorable for accumulation of higher pore pressures. After the high Vp/Vs values emerge, the subsequent foreshock-quiescence periods allow high pore pressures to continue diffusing along fault planes, without intermittent smaller events to disrupt the pore pressure buildup. The total diffusion distances eventually reach ~400 m and ~900 m prior to the two mainshocks. These distances are comparable to the estimated rupture lengths of ~300–700 m and ~700–1600 m for the M3.3 and M4.0 events, respectively, assuming stress-drop values range from 1–10 MPa, which is typical of tectonic and fluid-injection-induced earthquakes (Methods)[52,53]. The extent

of fluid diffusion throughout the nucleation phase during stages S2 and S3 likely controls the rupture size of the M3–M4 mainshocks. The pore pressure-controlled rupture sizes are consistent with both dynamic rupture simulations incorporating pore-pressure perturbations[54] and observations relating magnitude truncation of larger induced earthquakes to the stimulated volumes[55].

The prolonged nucleation phase also provides new insights into delayed triggering of induced earthquakes in HF settings. Previous studies have primarily attributed such delays to fluid diffusion from an injection point to a nucleation area[2,56,57]. Our study highlights an additional delay may be required for fluids to permeate and condition a fault patch for a larger event by sufficiently elevating the pore pressures on a fault patch of higher strength. The additional delay is governed by fluid diffusivity along the fault and the patch size amenable to pore pressure increase. The extra delays of a couple of days for the moderate earthquakes further support the observations that many large HF-induced earthquakes occur near or after the time of well completion[56,58]. This finding underscores the necessity to consider not only the magnitude of elevated pore pressure but also its spatial extent along the fault when analyzing triggering mechanisms of moderate to strong events.

In contrast to the M3.3 and M4.0 events, the M4.1 sequence exhibits continued foreshock activity, with neither a preceding quiescent interval nor an apparent migration pattern. A plausible explanation is that the seismogenic faults (F2 and F3) accommodating the M4.0 and M4.1 events are hydraulically connected, allowing fluids accumulated on F2 to migrate onto F3 during the suspension of HF after the occurrence of the first M4.0 event. This pre-injection pore-pressure buildup may have already partially conditioned F3 and facilitated faster nucleation of the M4.1 event. Aseismic slip serves as an alternative mechanism to explain the observed foreshock quiescence in M3.3 and M4.0 sequences[12,13]. However, we cannot differentiate whether aseismic slip is more likely in the M3.3 and M4.0 sequences than in the M4.1 sequence, because slow slip prior to large events can also produce seismic swarms[59,60]. Further information of casing deformation of HF wells or surface deformation may help to distinguish these mechanisms[61,62].

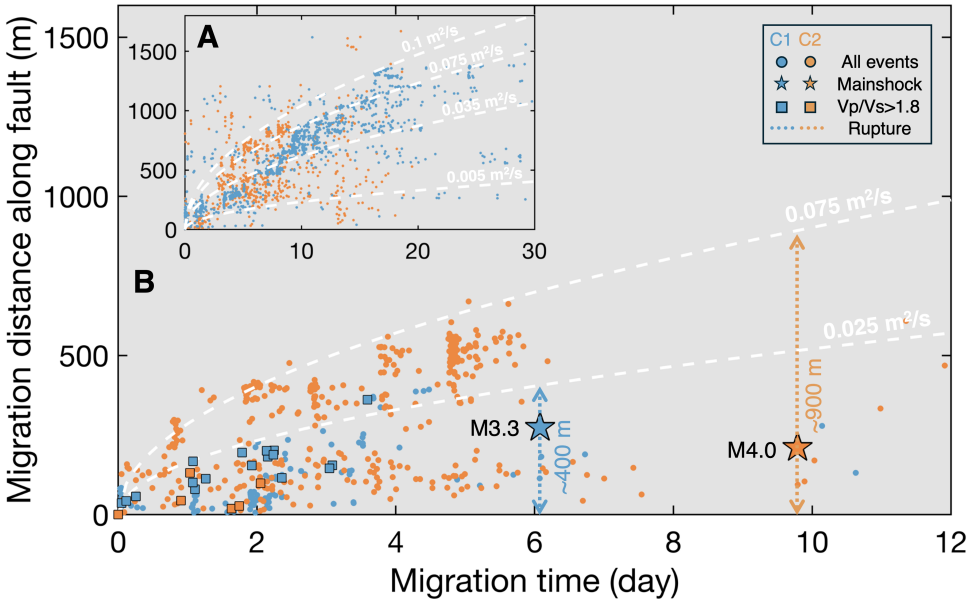

Fig. 5. Seismicity migration processes. (**A**) All seismicity in clusters C1 (blue dots) and C2 (orange dots). Migration time and distance are relative to the first event in each cluster. (**B**) Migration of seismicity within 150 m of the F1 (blue dots) and within 200 m of F2 (orange dots). The distance and time are relative to the first event with Vp/Vs >1.8 along each fault. Squares highlight the events associated with Vp/Vs >1.8. Stars mark the M3.3 and M4.0 mainshocks. Two vertical dotted double-headed arrows indicate the diffusion distances from the first event to the respective mainshocks along faults F1 and F2.

Dilatancy strengthening inhibits aftershocks

Large fluid-induced earthquakes are usually followed by abundant aftershocks[63,64]. In HF settings, such aftershock swarms have been reported for mainshocks across a wide magnitude range from M2 to M5[5,17,65]. In contrast, the M3.3 and M4.0 events in this study are followed by distinctly few aftershocks within their respective fault zones.

The paucity of aftershocks on fault segments with high porosity and elevated pore pressure may be explained by dilatancy strengthening, similar to that proposed for the rupture barrier zones of the Gofar transform fault[43]. High-rate coseismic slip can lead to temporary drop in pore pressures on a fault zone, thereby increasing the effective normal stress (clamping effect) that inhibits subsequent seismic events before pore pressure re-equilibrates with the ambient level[66,67]. In cluster C1, the second episode of seismicity associated with high Vp/Vs likely reflects recovery of high pore pressure

due to resumed HF and fault zone compaction after the M3.3 event. Notably, the estimated pore-pressure increases preceding the mainshock reach up to ~13–19 MPa, suggesting that the background stress is tens of MPa from failure in the absence of overpressure. Such a stable background stress regime is consistent with the observed aftershock quiescence and the absence of a second M>3 event when injection resumed ~35 days later.

Potential of real-time seismic hazard assessment and mitigation

We observe a consistent pattern of elevated *in-situ* Vp/Vs preceding the M>3 induced earthquakes, suggesting that a near-real-time operational workflow for intervention could be developed for seismic hazard mitigation across diverse anthropogenic fluid-injection settings, such as unconventional hydrocarbon recovery, enhanced geothermal systems, and geological CO_2 storage (Fig. 6).

First, we identify a lead time of ~5–10 days between the onset of elevated Vp/Vs and the eventual M3–M4 mainshocks, which indicates a prolonged nucleation phase of fluid diffusion and accumulation prior to rupture. Given the stable Vp/Vs estimates with high spatiotemporal resolution of ~2 days and ~150 m, this nucleation process provides a valuable window for operators to implement mitigation strategies to reduce the likelihood of larger events in HF settings, for both shale gas development and enhanced geothermal systems.

Second, the *in-situ* Vp/Vs measurements are independent of earthquake magnitude (Supplementary Fig. 5), enabling assessment of near-source pore pressure using only small-magnitude events. By contrast to the conventional traffic-light protocols based on earthquake magnitude[68], our modified *in-situ* Vp/Vs approach provides more precise timing for intervention by indicating when near-source pore pressure has increased to a high level (e.g., ~13–19 MPa for Vp/Vs ~1.8 using the effective-stress framework). This approach would be in particular effective for magnitude-jump scenarios where $M \geq 4$ events occur without preceding M2 yellow-light events, as is the case for ~30% of the earthquakes in both our study area and the Western Canada Sedimentary Basin[5,68], both of which are experiencing severe HF-induced seismic hazard[4,7]. The magnitude-

independent monitoring strategy is also well suited to estimate the pore pressure evolution in geological CO_2 storage reservoirs, where induced seismicity remains confined to small magnitudes[69].

Third, the 4G seismic network used in our study can transmit waveform data with latencies of less than 1 minute, providing reliable data streams for near-real-time Vp/Vs analysis. Consistent with this capability, we show that a 48-station array can achieve a spatiotemporal Vp/Vs resolution of 3 days and 200 m for a seismicity cluster with an average event spacing of ~20 m. Denser monitoring systems, such as the Toc2ME array in northeastern British Columbia, Canada[70], or networks enabled by Distributed Acoustic Sensing[71], are expected to further enhance the spatiotemporal resolution and shorten the response time for intervention.

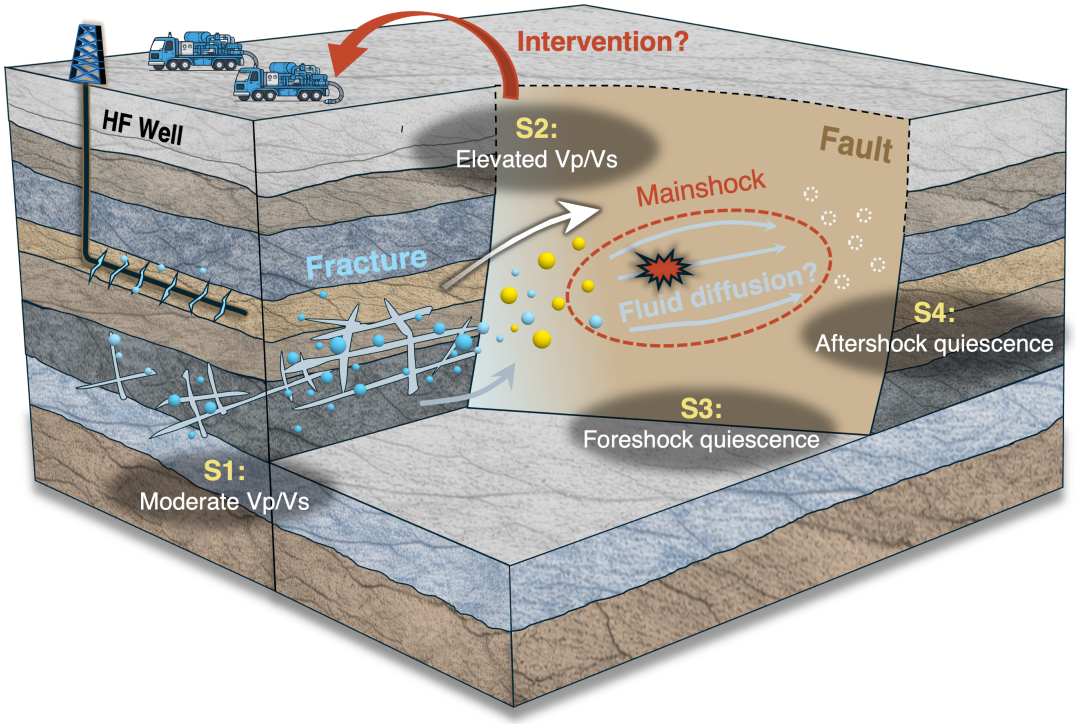

Fig. 6. Conceptual model of spatiotemporal Vp/Vs evolution. Blue spheres represent earthquakes on the hydraulic fractures, showing moderate Vp/Vs values during Stage S1. Yellow spheres denote earthquakes migrating onto a nearby pre-existing fault, exhibiting elevated Vp/Vs values in Stage S2. The onset of elevated Vp/Vs triggers intervention in HF operation. Light-blue arrows represent inferred fluid diffusion in Stage S3. Red star indicates the mainshock hypocenter with the red dashed oval outlining the rupture area. Dashed white circles highlight the paucity of aftershocks in Stage S4.

Methods

Seismicity Catalogue

The data for the two seismic clusters analyzed in this study are from two separate seismic monitoring networks. Cluster C1 was monitored by a short-term dense seismic nodal array consisting of 336 stations operating between February 28 and May 8, 2019 (Fig. 1)[31]. Cluster C2 was monitored by a long-term seismic network consisting of 48 4G stations that transmit waveform in real time (hereafter referred to as the 4G seismic network)[32]. The 4G seismic network was first equipped with 40 stations and was deployed between October 2022 and June 2023. The network was expanded to 48 stations in June 2023, and is still operational.

Xu et al.[31] developed an enhanced catalogue including cluster C1 by applying the deep-learning-based picker PhaseNet[72] to automatically obtain P- and S-wave arrivals from 100-Hz continuous seismic records. The outliers in picked arrivals were removed by assuming a quasilinear moveout with epicentral distance (Pearson correlation > 0.9), and only high-quality arrivals were retained with at least 50 P- and 30 S-arrivals per event. The initial event locations were determined with the probabilistic, non-linear location algorithm NonLinLoc[73] using a 1D velocity model derived from ambient-noise tomography[5], yielding 14,436 events with mean uncertainties of ~70 m horizontally and ~120 m vertically. The hypocenters were then refined using the double-difference method HypoDD[74] with differential times determined by waveform cross correlation, yielding a final catalog of 13,885 events with magnitudes ranging from M-1.7 to M3.3. Bootstrapping tests indicate relocation uncertainties of less than 50 m for most events.

For cluster C2[32], a re-trained PhaseNet using local earthquakes in Changning was applied to pick P- and S-arrivals. A 2-s time window centered on the median P arrival was used to remove abnormal picks. Between July 2022 and July 2023, the array detected over 14,000 earthquakes, where 5,000 occurred in cluster C2. Ye et al.[32] determines initial event locations using NonLinLoc[73] and the same velocity model as for cluster C1. The locations are then refined with differential times determined by wave cross correlations using a double-difference method[74]. Relocation uncertainties are ~70 m horizontally and ~100 m vertically, assessed by 100 bootstrap tests.

Focal mechanism solutions

This study includes six focal mechanism solutions (FMS) for the mainshocks in total: the M3.3 event in cluster C1 and five M4-class events in cluster C2 (Figs. 1E, 1F). The FMS for the M3.3 event is from Xu et al.[31], using first-motion polarities and S/P amplitude ratios measured by the short-term dense array. The M4.0, M4.3, M4.5, and M4.9 events in cluster C2 are obtained from the National Earthquake Data Center (NEDC) focal-mechanism catalogue (https://data.earthquake.cn/datashare/report.shtml?PAGEID=earthquake_dzzyjz), which are estimated by waveform inversion using broadband stations within 200 km.

The FMS for the M4.1 event is not available in the official NEDC focal-mechanism catalogue. We therefore calculate a solution using the Time-Domain Moment Tensor inversion (TDMT) approach[75] (Supplementary Fig. 6), by minimizing the L2-norm misfit between observed and synthetic three-component waveforms. We use the full body and surface waveforms from 22 broadband stations within 200 km epicentral distance and bandpass filtered the data to 0.02–0.1 Hz. Synthetic Green's functions are computed with an F-K (frequency-wavenumber) method using a 1-D layered velocity structure extracted from CRUST1.0 in the study region. We perform a depth search and obtain a best-fitting centroid depth at 3 km, consistent with the hypocentral depth of 2.8 km derived from the enhanced catalogue in Ye et al.[32].

Time-lapse In-situ Vp/Vs analysis

The earthquake cluster-based *in-situ* Vp/Vs analysis was first developed by Lin and Shearer[25]. This method does not explicitly rely on earthquake locations, nor does it involve an inversion process like travel time tomography. Instead, it is based solely on the relative P- and S-wave arrival time differences between event pairs, and therefore depends directly on the phase-picking quality. The basic principle of this method follows a differential approach (Supplementary Fig. 7). If a pair of events occurs in proximity and are recorded at a distant station so that the ray paths are essentially identical, then the ratio between the differential S-wave and differential P-wave travel times corresponds to the local Vp/Vs at the source of the event pair. For multiple

recording stations, the differential arrival data align along a straight line, the slope of which yields the *in-situ* Vp/Vs ratio[25]. We present the basic derivation of the method below.

For an event pair (event 1 and 2) in proximity, the travel time differences of P (δT_P) and S waves (δT_S) at a station i from can be expressed as:

$$\delta {T_P}^i = T_{P2}^i - T_{P1}^i = \frac{\delta l_P^i}{V_P}, \tag{1}$$

$$\delta T_S^i = T_{S2}^i - T_{S1}^i = \frac{\delta l_S^i}{V_S}, \tag{2}$$

where T_{P1}^i and T_{P2}^i denote the P-wave travel times of event 1 and 2, respectively, δl_P^i represents the difference in the P-wave ray-path lengths, and V_P is the P-wave velocity at the source region. Analogous definitions apply for the S wave. Given the P- and S-wave ray paths are identical for nearby events, i.e., $\delta l_P^i = \delta l_S^i$, the two equations can be combined:

$$\frac{V_P}{V_S} = \frac{\delta T_S^i}{\delta T_P^i}. \tag{3}$$

Lin and Shearer[25] did not use differential travel-time data δT_P^i and δT_S^i directly. Instead, they used the manually picked absolute arrival times. Since an arrival time can be decomposed into the origin time and the travel time, we have:

$$\begin{aligned} \delta t_P^i = t_{P2}^i - t_{P1}^i &= \left(t_{o2} + T_{P2}^i\right) - \left(t_{o1} + T_{P1}^i\right) \\ &= (t_{o2} - t_{o1}) + \left(T_{P2}^i - T_{P1}^i\right) = \delta t_o + {\delta T_P}^i, \end{aligned} \tag{4}$$

$$\begin{aligned} \delta t_S^i = t_{S2}^i - t_{S1}^i &= \left(t_{o2} + T_{S2}^i\right) - \left(t_{o1} + T_{S1}^i\right) \\ &= (t_{o2} - t_{o1}) + \left(T_{S2}^i - T_{S1}^i\right) = \delta t_o + {\delta T_S}^i, \end{aligned} \tag{5}$$

where δt_P^i is the differential P-wave arrival times of event 1 (t_{P1}^i) and event 2 (t_{P2}^i) and δt_o is the differential origin time of event 1 (t_{o1}) and event 2 (t_{o1}). Analogous definitions apply for the S wave. By combining the five equations for travel-time differences and arrival-time differences, we obtain:

$$\delta t_S^i = \left(\frac{V_P}{V_S}\right) \delta t_P^i + \delta t_o \left(1 - \frac{V_P}{V_S}\right). \tag{6}$$

In practice, the differential arrival times at multiple stations constitute a straight line with slope equal to the Vp/Vs ratio and the intercept proportional to the origin-time

offset (Supplementary Fig. 6). Since the intercept is not of interest, it can be removed by subtracting the mean value for each event pair so that we can combine multiple event pairs with different origin times to further improve stability. Due to picking errors, the differential arrival times typically scatter around the ideal line of theoretical Vp/Vs and exhibit a spindle shape. Stable estimation of Vp/Vs are therefore obtained by fitting multiple event pairs within a defined event cluster. The resulting Vp/Vs represents an average value over the aperture of the selected cluster, introducing the concept of spatial resolution.

In this study, we take a slightly different technical route from Lin and Shearer[25] by using travel times directly instead of arrival times. Although travel times depend on both location results and event origin times, subtracting the mean of the differential travel times yields results identical to those derived from demeaned arrival times (Text S1).

Additionally, we improve the spatiotemporal resolution by introducing a moving-window strategy in the workflow. For each event, we group nearby events with high waveform similarity (>0.85) within a specified time window (2–3 days) and spatial range (150–200 m). After fitting the measured travel time differences, the resolved Vp/Vs value of the clustered seismicity will be assigned to the target event if it satisfies the uncertainty threshold (see details below). In theory, we can derive a Vp/Vs value for each earthquake, and therefore obtain the time-lapse, *in-situ* Vp/Vs values with the evolution of a seismic sequence.

Taking cluster C1 as an example, the detailed processing workflow is described in detail (Supplementary Fig. 8).

Step 1: Database construction. A differential travel-time database is established containing all possible event pairs. Event pairs with hypocentral separation less than L=150 m and origin-time difference within T=2 days are selected to calculate the P- and S-wave waveform cross-correlation coefficients. Waveforms are filtered in the 4–10 Hz band at a 100 Hz sampling rate, with window lengths of 0.4 s for P waves and 0.7 s for S waves. We retain cross-correlation coefficients if they satisfy the following criteria: (1) the source-station distance is greater than 5 km to ensure P- and S-wave

takeoff angle differences below 0.5°[27]; (2) Each event pair shares at least 10 stations with both P- and S-wave differential times to ensure stability; (3) P- and S-wave cross-correlation coefficients are ≥ 0.85 to guarantee sufficient waveform similarity. Waveform cross-correlation plays a key role in correcting travel-time differences as illustrated in Supplementary Fig. 9.

Step 2: Sub-cluster definition. For each earthquake, a local sub-cluster is defined as all events occurring within a spatiotemporal window of L=150 m and T=±2 days for the target event (Supplementary Fig. 10). We retain subclusters with more than 30 events and more than 100 travel-time measurements for further analysis. We extract cross-correlation coefficients for all event pairs within the sub-cluster from the differential travel-time database constructed in Step 1. To obtain stable Vp/Vs estimates in regions with strong local variability, sub-clusters with appropriate geometric characteristics are selected[25]. Principal Component Analysis (PCA) is applied to the covariance matrix of event locations within each sub-cluster to assess isotropy, with eigenvalues $\lambda_1 \geq \lambda_2 \geq \lambda_3$. Sub-clusters with $\lambda_1/\lambda_3 \leq K$ $(K = 35)$ are considered approximately spherical and retained for analysis. For each event, we define a sub-cluster by applying the spatiotemporal moving window to obtain a corresponding Vp/Vs value.

Step 3: Preprocessing. We remove outliers of differential travel-time data before slope fitting. We use three methods: least squares (LS), Huber regression (L1-L2), and random sample consensus (RANSAC). RANSAC behaves as iteratively fitting random subsets and selecting the model best fitting the full dataset, which is found most effective for our dataset (Supplementary Fig. 11). After outlier removal, the mean of P- and S-wave travel-time differences in each event pair is subtracted to correct potential origin-time offsets. We find some incorrect P-wave phase picking due to low signal-to-noise ratio will result in travel time difference anomalies near $\Delta t_s = 0$ (Supplementary Fig. 12). We therefore apply an additional procedure to remove these outliers.

Step 4: Iterative fitting. We apply a total least squares (TLS) fitting to the preprocessed travel-time differences (Supplementary Fig. 13). We iteratively remove

50 measurements with the largest residuals in each iteration until convergence: the maximum residual is less than twice the standard deviation, and at least 100 points remain. After iterative fitting, we compile statistics on the number of retained events and travel-time data points in each sub-cluster. We ensure each sub-cluster includes at least 30 events, where most sub-clusters contain more than 1,000 differential travel-time data points (Supplementary Fig. 14). We also note that conventional LS fitting would underestimate Vp/Vs, as both P- and S-wave differential times contain measurement errors (Supplementary Fig. 15)[25].

Step 5: Stability testing. Three tests are conducted. First, bootstrapping tests assess the uncertainty by resampling 90% of events 100 times per sub-cluster, with standard deviation used to quantify uncertainty (Supplementary Fig. 16c). Second, synthetic tests that use a layered velocity model with a gradient Vp/Vs model varying from 1.78 to 1.73 (Supplementary Fig. 17) assess robustness against heterogeneity and data distribution (Supplementary Fig. 16d). Sub-clusters with uncertainties > 0.02 or theoretical deviations > 0.01 are excluded. The same tests are also applied to cluster C2 (Supplementary Fig. 18). For cluster C1, sub-clusters are defined with a spatial radius of three times of relocation uncertainty L = 150 m, and with a time window T = 2 days to balance time resolution and stability. A third sensitivity test using varying time windows (1–3 days) and radii (100–200 m) indicate that spatial range has a stronger effect on influencing the results than temporal range (Supplementary Fig. 19). A radius of 150 m and T = 2 days is adopted to capture the rupture scale of the largest event (M3.3, ~300 m). We use L = 200 m and T = 3 days to improve result stability in Cluster C2 with fewer stations and larger relocation uncertainties (Supplementary Fig. 20).

Estimation of porosity change

In this study, we apply two approaches to compute theoretical Vp/Vs for porous rocks, the Kuster-Toksöz theoretical crack model[38] and the self-consistent method[39]. The Kuster-Toksöz crack model analyzes seismic-wave propagation in porous rocks using scattering theory. The effective elastic moduli of porous rocks can be solved by assuming an equivalent homogeneous medium that can generate a scattered wavefield

matching the actual one caused by multiple pores embedded in the host rock. This approach assumes sparse pores, long wavelengths relative to pore size, and negligible multiple scattering effects, and can provide analytical formulas for effective moduli for various pore shapes and host rocks. The self-consistent method similarly derives effective elastic moduli from scattering theory but differs conceptually from the Kuster-Toksöz model. It does not assume separate effective medium to model the actual wavefield, instead, it iteratively adjusts the elastic parameters of host rocks until the scattered wavefield of multiple pores is nullified, yielding the equivalent porous rock properties. This method is better suited for high-porosity rocks but requires iterative solutions due to the nonlinear nature of the governing equations.

Based on the regional ambient-noise tomographic result[5] and well logs[76], we assume $V_P = 5200\,m/s$, $V_S = 3000\,m/s$, $\rho = 2700\,kg/m^3$ for the seismogenic carbonate formation, and $V_P = 1500m/s$, $V_S = 0m/s$, $\rho = 1000kg/m^3$ for the pore-filling treatment fluid. The porosity varies between 0.001 and 0.3 and the pore aspect ratio varies from 0.01 to 0.1 in calculation of the theoretical Vp/Vs range (Fig. 4B). Results show close agreement at low porosity with absolute differences less than 0.01. At high porosity (porosity exceeding aspect ratio), only the self-consistent method is valid. The Hashin-Shtrikman bounds are used to constrain the theoretical upper and lower limits of the effective elastic properties[27].

Estimation of pore pressure variation

Laboratory measurements of elastic wave velocities as a function of pore pressure provide the foundation for relating observed Vp/Vs changes to pore-pressure perturbations[44], where Vp and Vs of multiple sedimentary rock samples were measured under varying pore pressure and confining stress conditions. Based on these laboratory relationships, pore-pressure changes are inferred from the resolved Vp/Vs values in this study with specific confining stress at the seismogenic depth. We use the depth-dependent stress regime estimated in Tan et al.[20] as the baseline, which is derived from focal mechanism solutions and over pressure measurements. At the hypocentral depth of ~2.8 km for the M4.1 event, we regard the vertical principal stress ~66 MPa as the

confining stress and initial pore pressure of ~42 MPa before injection. During the foreshock sequence of the M4.1 event, the observed Vp/Vs increases from 1.73 to 1.80 (i.e., by ~4%). With the specific confining stress of ~66 MPa, the corresponding Vp and Vs values can be derived for varied pore pressure values (Supplementary Fig. 21). A 4% increase in Vp/Vs corresponds to pore-pressure increase of 18.9, 13, or 13.1 MPa for three representative sedimentary rock samples (Supplementary Fig. 21). Based on this relationship, we estimate the pore pressure changes for different Vp/Vs values (Fig. 4C).

Calculation of fluid diffusivity

We follow the practice in Shapiro[18] to estimate the fluid diffusivity by fitting the seismicity migration fronts:

$$r = \sqrt{4\pi D t}\,, \tag{7}$$

where r is the diffusion distance, D is the diffusivity value and t is the diffusion time. To estimate the fluid diffusivity inferred from seismicity migration in cluster C1 and C2, we take the first event in each cluster as the spatiotemporal reference to compute the diffusion times and distances for subsequent events. Four theoretical diffusion fronts with diffusivities of 1, 0.075, 0.035 and 0.005 m^2/s are shown as references in Fig. 5A. We also estimate the fluid diffusivity along the seismogenic faults F1 and F2 using the events within 150 m and 200 m to the faults, respectively. We take the first event with high Vp/Vs > 1.8 along each fault as the reference point to calculate the diffusion time and distance. Two diffusion fronts with diffusivities of 0.075 and 0.025 m^2/s are shown in Fig. 5B.

Estimation of earthquake rupture size

We calculate the rupture radius of the M3.3 and M4.0 events by assuming a circular crack model:

$$\Delta\sigma = \frac{7}{16}\frac{M_0}{a^3}\,, \tag{8}$$

where a denotes the radius of the rupture, M_0 denotes seismic moment, and $\Delta\sigma$ represents the stress drop. Assuming that the stress drop is within 1–10 MPa, which is common for both tectonic and induced earthquakes[52,53], we estimate the rupture

diameters ($2a$) for the M3.3 and M4.0 events to be 300–700 m and 700–1600 m, respectively.

References

1. Ellsworth, W. L. Injection-Induced Earthquakes. *Science* **341**, 1225942 (2013).
2. Bao, X. & Eaton, D. W. Fault activation by hydraulic fracturing in western Canada. *Science* **354**, 1406–1409 (2016).
3. Lei, X., Wang, Z. & Su, J. The December 2018 ML 5.7 and January 2019 ML 5.3 Earthquakes in South Sichuan Basin Induced by Shale Gas Hydraulic Fracturing. *Seismol. Res. Lett.* **90**, 1099–1110 (2019).
4. Atkinson, G. M., Eaton, D. W. & Igonin, N. Developments in understanding seismicity triggered by hydraulic fracturing. *Nat. Rev. Earth. Environ.* **1**, 264–277 (2020).
5. Li, J. *et al.* High seismic velocity structures control moderate to strong induced earthquake behaviors by shale gas development. *Commun. Earth. Environ.* **4**, 188 (2023).
6. Lu, R. *et al.* Seismogenic fault of the 2021 Ms 6.0 Luxian induced earthquake in the Sichuan basin, China constrained by high-resolution seismic reflection and dense seismic array. *Journal of Structural Geology* 105050 (2024).
7. Schultz, R. *et al.* Hydraulic Fracturing-Induced Seismicity. *Rev. Geophys.* **58**, (2020).
8. Keranen, K. M., Weingarten, M., Abers, G. A., Bekins, B. A. & Ge, S. Sharp increase in central Oklahoma seismicity since 2008 induced by massive wastewater injection. *Science* **345**, 448–451 (2014).
9. Galloway, E., Hauck, T., Corlett, H., Pană, D. & Schultz, R. Faults and associated karst collapse suggest conduits for fluid flow that influence hydraulic fracturing-induced seismicity. *Proc. Natl. Acad. Sci. U.S.A.* **115**, (2018).
10. Segall, P. & Lu, S. Injection-induced seismicity: Poroelastic and earthquake nucleation effects. *J. Geophys. Res. Solid Earth* **120**, 5082–5103 (2015).
11. Deng, K., Liu, Y. & Harrington, R. M. Poroelastic stress triggering of the December 2013 Crooked Lake, Alberta, induced seismicity sequence. *Geophys. Res. Lett.* **43**, 8482–8491 (2016).
12. Guglielmi, Y., Cappa, F., Avouac, J.-P., Henry, P. & Elsworth, D. Seismicity triggered by fluid injection–induced aseismic slip. *Science* **348**, 1224–1226 (2015).
13. Eyre, T. S. *et al.* The role of aseismic slip in hydraulic fracturing–induced seismicity. *Sci. Adv.* **5**, eaav7172 (2019).

14. Keranen, K. M. & Weingarten, M. Induced seismicity. *Annu. Rev. Earth Planet. Sci.* **46**, 149–174 (2018).

15. Ge, S. & Saar, M. O. Review: Induced seismicity during geoenergy development—A gydromechanical perspective. *J. Geophys. Res. Solid Earth* **127**, e2021JB023141 (2022).

16. Moein, M. J. A. *et al.* The physical mechanisms of induced earthquakes. *Nat. Rev. Earth. Environ.* **4**, 847–863 (2023).

17. Igonin, N., Verdon, J. P., Kendall, J. -Michael & Eaton, D. W. Large-scale fracture systems are permeable pathways for fault activation during hydraulic fracturing. *J. Geophys. Res. Solid Earth,* **126**, e2020JB020311 (2021).

18. Shapiro, S. A., Rothert, E., Rath, V. & Rindschwentner, J. Characterization of fluid transport properties of reservoirs using induced microseismicity. *Geophysics* **67**, 212–220 (2002).

19. He, L. *et al.* Detailed 3D seismic velocity structure of the Prague, Oklahoma fault zone and the implications for induced seismicity. *Geophys. Res. Lett.* **48**, e2021GL096137 (2021).

20. Tan, Y. *et al.* Tomographic evidences for hydraulic fracturing induced seismicity in the Changning shale gas field, southern Sichuan Basin, China. *Earth Planet. Sci. Lett.* **605**, 118021 (2023).

21. Tonegawa, T., Takemura, S., Yabe, S. & Yomogida, K. Fluid migration before and during slow earthquakes in the shallow Nankai subduction zone. *J. Geophys. Res. Solid Earth* **127**, e2021JB023583 (2022).

22. Tan, Y. *et al.* Hydraulic fracturing induced seismicity in the southern Sichuan Basin due to fluid diffusion inferred from seismic and injection data analysis. *Geophys. Res. Lett.* **47**, e2019GL084885 (2020).

23. Mao, S., Ellsworth, W. L., Zheng, Y. & Beroza, G. C. Depth-dependent seismic sensing of groundwater recovery from the atmospheric-river storms of 2023. *Science* **387**, 758–763 (2025).

24. Sun, T. *et al.* Pronounced temporal velocity variations within the fault fracture zone in response to Earth tide modes. *Natl. Sci. Rev.* **12**, nwaf023 (2025).

25. Lin, G. & Shearer, P. Estimating local Vp/Vs ratios within similar earthquake clusters. *Bull. Seismol. Soc. Am.* **97**, 379–388 (2007).

26. Liu, T., Gong, J., Fan, W. & Lin, G. In-situ Vp/Vs reveals fault-zone material variation at the westernmost Gofar transform fault, east Pacific Rise. *J. Geophys. Res. Solid Earth* **128**, e2022JB025310 (2023).

27. Roth, M. P., Verdecchia, A., Harrington, R. & Liu, Y. Inferring rock strength and fault activation from high-resolution in situ Vp/Vs estimates surrounding induced earthquake clusters. *Seismica* **2**, (2023).

28. Zou C. *et al.* Shale gas in China: characteristics, challenges and prospects (II). *Petroleum Exploration and Development* **43**, 166–178 (2016).

29. Xiao, H. *et al.* The identification of micro-faults at the bottom of Wufeng Formation in Changning Area and its influence on shale gas development. *China Mining Magazine* **31**, 171–180 (2022).

30. An, M. *et al.* Brittle sedimentary strata focus a multimodal depth distribution of seismicity during hydraulic fracturing in the Sichuan Basin, Southwest China. *Tectonophysics* **880**, 230332 (2024).

31. Xu, J. *et al.* Shallow lingering and deep transient seismicity related to hydraulic fracturing in the Changning Shale Gas Field, Sichuan Basin, China. *J. Geophys. Res. Solid Earth* **130**, e2024JB030279 (2025).

32. Ye, Y. *et al.* Data for: Injected Fluids Both Trigger and Facilitate a Cascade of Larger Earthquake Ruptures, Zenodo (2025). doi:10.5281/zenodo.13945413.

33. Tatham, R. H. Vp/Vs and lithology. *Geophysics* **47**, 336–344 (1982).

34. Eberhart-Phillips, D., Han, D. H. & Zoback, M. D. Empirical relationships among seismic velocity, effective pressure, porosity, and clay content in sandstone. *Geophysics* **54**, 82–89 (1989).

35. Christensen, N. I. Poisson's ratio and crustal seismology. *J. Geophys. Res.* **101**, 3139–3156 (1996).

36. Anyiam, U. O., Qian, J., Tan, Y. & Zhang, H. Comprehensive seismic evidence for the inducing mechanism of extremely shallow 2019 Changning Ms 6.0 earthquake by solution salt mining, Sichuan Basin, China. *Geology* **52**, 441-446 (2024)

37. Allam, A. A., Ben-Zion, Y., Kurzon, I. & Vernon, F. Seismic velocity structure in the Hot Springs and Trifurcation areas of the San Jacinto fault zone, California, from double-difference tomography. *Geophys. J. Int.* **198**, 978–999 (2014).

38. Kuster, G. T. & Toksöz, M. N. Velocity and attenuation of seismic waves in two-phased media: Part I. Theoretical formulations. *Geophysics* **39**, 587–606 (1974)

39. Berryman, J. G. Long-wavelength propagation in composite elastic media I. Spherical inclusions. *J. Acoust. Soc. Am.* **68**, 1809–1819 (1980).

40. Douma, J. & Crampin, S. The effect of a changing aspect ratio of aligned cracks on shear wave vertical seismic profiles: A theoretical study. *J. Geophys. Res.* **95**, 11293–11300 (1990).

41. Mishra, O. P. & Zhao, D. Crack density, saturation rate and porosity at the 2001 Bhuj, India, earthquake hypocenter: a £uid-driven earthquake? *Earth. Planet. Sci. Lett.* **212**, 393-405 (2003)

804 42. Roland, E., Lizarralde, D., McGuire, J. J. & Collins, J. A. Seismic velocity
805 constraints on the material properties that control earthquake behavior at the
806 Quebrada-Discovery-Gofar transform faults, East Pacific Rise. *J. Geophys. Res.*
807 **117**, 2012JB009422 (2012).

808 43. Liu, Y., McGuire, J. J. & Behn, M. D. Aseismic transient slip on the Gofar
809 transform fault, East Pacific Rise. *Proc. Natl. Acad. Sci. U.S.A.* **117**, 10188–
810 10194 (2020).

811 44. Christensen, N. I. "Pore pressure, seismic velocities, and crustal structure" in
812 *Geophysical Framework of the Continental United States*, L. C. Pakiser and W.
813 D. Mooney, Eds. (Geological Society of America, Boulder, CO, 1989), pp. 783–
814 798.

815 45. Xu, X., Hofmann, R., Batzle, M. & Tshering, T. Influence of pore pressure on
816 velocity in low-porosity sandstone: Implications for time-lapse feasibility and
817 pore-pressure study. *Geophysical Prospecting* **54**, 565–573 (2006).

818 46. Lay, T. & Kanamori, H. An asperity model of large earthquake sequences.
819 *Earthquake prediction: An international review* **4**, 579–592 (1981).

820 47. Aki, K. Asperities, barriers, characteristic earthquakes and strong motion
821 prediction. *J. Geophys. Res.* **89**, 5867–5872 (1984).

822 48. McGarr, A. Maximum magnitude earthquakes induced by fluid injection: Limits
823 on fluid injection earthquakes. *J. Geophys. Res. Solid Earth* **119**, 1008–1019
824 (2014).

825 49. Pei, S., Zhang, H., Su, J. & Cui, Z. Ductile gap between the Wenchuan and
826 Lushan earthquakes revealed from the two-dimensional Pg seismic tomography.
827 *Sci. Rep.* **4**, 6489 (2014).

828 50. Wang, Z., Su, J., Liu, C. & Cai, X. New insights into the generation of the 2013
829 Lushan Earthquake (Ms7.0), China: 2013 Lushan earthquake generation. *J.*
830 *Geophys. Res. Solid Earth* **120**, 3507–3526 (2015).

831 51. Rice, J. R. Heating and weakening of faults during earthquake slip. *J. Geophys.*
832 *Res.* **111**, 2005JB004006 (2006).

833 52. Huang, Y., Ellsworth, W. L. & Beroza, G. C. Stress drops of induced and tectonic
834 earthquakes in the central United States are indistinguishable. *Sci. Adv.* **3**,
835 e1700772 (2017).

836 53. Allmann, B. P. & Shearer, P. M. Global variations of stress drop for moderate to
837 large earthquakes. *J. Geophys. Res.* **114**, 2008JB005821 (2009).

838 54. Galis, M., Ampuero, J. P., Mai, P. M. & Cappa, F. Induced seismicity provides
839 insight into why earthquake ruptures stop. *Sci. Adv.* **3**, eaap7528 (2017).

55. Shapiro, S. A., Krüger, O. S., Dinske, C. & Langenbruch, C. Magnitudes of induced earthquakes and geometric scales of fluid-stimulated rock volumes. *Geophysics* **76**, WC55–WC63 (2012).

56. Gao, D. *et al.* Complex 3D migration and delayed triggering of hydraulic fracturing-induced seismicity: A case study near Fox Creek, Alberta. *Geophys. Res. Lett.* **49**, e2021GL093979 (2022).

57. Fasola, S. L. *et al.* Hydraulic fracture injection strategy influences the probability of earthquakes in the Eagle Ford Shale Play of South Texas. *Geophys. Res. Lett* **46**, 12958–12967 (2019).

58. Peña Castro, A. F. *et al.* Stress chatter via fluid flow and fault slip in a hydraulic fracturing-induced earthquake sequence in the Montney Formation, British Columbia. *Geophys. Res. Lett* **47**, e2020GL087254 (2020).

59. Kato, A. *et al.* Propagation of slow slip leading ip to the 2011 Mw 9.0 Tohoku-Oki earthquake. *Science* **335**, 705–708 (2012).

60. Ruiz, S. *et al.* Intense foreshocks and a slow slip event preceded the 2014 Iquique M_w 8.1 earthquake. *Science* **345**, 1165–1169 (2014).

61. Zoback, M. D., Kohli, A., Das, I. & McClure, M. "The importance of slow slip on faults during hydraulic fracturing stimulation of shale gas reservoirs," in *SPE Americas Unconventional Resources Conference* (Society of Petroleum Engineers, Pittsburgh, PA, USA, 2012), Paper SPE-155476-MS. doi:10.2118/155476-MS.

62. Eyre, T. S., Samsonov, S., Feng, W., Kao, H. & Eaton, D. W. InSAR data reveal that the largest hydraulic fracturing-induced earthquake in Canada, to date, is a slow-slip event. *Sci. Rep.* **12**, 2043 (2022).

63. Yu, H., Wang, B. & Meng, H. Advances in fluid injection-induced earthquakes research and their implications for seismic source physics. *Chinese Journal of Geophysics* **68**, 2962–2992 (2025).

64. Ellsworth, W. L., Giardini, D., Townend, J., Ge, S. & Shimamoto, T. Triggering of the Pohang, Korea, Earthquake (Mw5.5) by Enhanced Geothermal System Stimulation. *Seismological Research Letters*, **90**, 1844–1858. (2019).

65. Clarke, H., Verdon, J. P., Kettlety, T., Baird, A. F. & Kendall, J. Real-time imaging, forecasting, and management of human-induced seismicity at Preston New Road, Lancashire, England. *Seismological Research Letters*, **90**, 1902-1915 (2019).

66. Segall, P. & Rice, J. R. Dilatancy, compaction, and slip instability of a fluid-infiltrated fault. *J. Geophys. Res.* **100**, 22155–22171 (1995).

67. Brantut, N. Dilatancy-induced fluid pressure drop during dynamic rupture: Direct experimental evidence and consequences for earthquake dynamics. *Earth. Planet. Sci. Lett.* **538**, 116179 (2020).

68. Kao, H., Visser, R., Smith, B. & Venables, S. Performance assessment of the induced seismicity traffic light protocol for northeastern British Columbia and western Alberta. *The Leading Edge* **37**, 117–126 (2018).

69. White, D., Daley, T. M., Paulsson, B. & Harbert, W. Borehole seismic methods for geologic CO2 storage monitoring. *The Leading Edge* **40**, 434–441 (2021).

70. Eaton, D. W. *et al.* Induced seismicity characterization during hydraulic-fracture monitoring with a shallow-wellbore geophone array and broadband sensors. *Seismol. Res. Lett.* **89**, 1641–1651 (2018).

71. Chamarczuk, M. *et al.* Insights into seismicity associated with flexibly operating enhanced geothermal system from real-time distributed acoustic sensing. *J. Geophys. Res. Solid Earth* **130**, e2025JB031634 (2025).

72. Zhu, W. & Beroza, G. C. PhaseNet: A Deep-neural-network-based seismic arrival time picking method. *Geophys. J. Int.* **216**, 261-273 (2018).

73. Lomax, A., Virieux, J., Volant, P. & Berge-Thierry, C. Probabilistic earthquake location in 3D and layered models: Introduction of a Metropolis-Gibbs method and comparison with linear locations. *Advances in seismic event location* 101–134 (2000).

74. Waldhauser, F. A Double-Difference Earthquake Location Algorithm: Method and Application to the Northern Hayward Fault, California. *Bull. Seismol. Soc. Am.* **90**, 1353–1368 (2000).

75. Dreger, D. S. & Helmberger, D. V. Determination of source parameters at regional distances with three-component sparse network data. *J. Geophys. Res.* **98**, 8107–8125 (1993).

76. Ma, X. *et al.* Lithology-controlled stress variations of Longmaxi shale–Example of an appraisal wellbore in the Changning area. *Rock Mechanics Bulletin* **1**, 100002 (2022).

Data availability

The seismicity catalogues, focal mechanism solutions and Vp/Vs results in this study can be downloaded at https://doi.org/10.5281/zenodo.18396545.

Acknowledgments

We thank H. Dong and H. Yu for helpful discussions.

Funding

Natural Sciences and Engineering Research Council of Canada Discovery Grant RGPIN-2024-05737 (JX, YJL)

National Natural Science Foundation of China, Grant U2139204 (JLL, JX)

National Natural Science Foundation of China, Grant 42488301 (JLL)

National Key Research and Development Project of China, Grant 2022YFF0800701 (JLL)

Author contributions

Conceptualization: JX, YJL, RMH, JLL

Methodology: JX, MPR, YCH

Data and Resources: YJL, JLL, RMH

Visualization: JX

Supervision: YJL, JLL, RMH

Writing—original draft: JX

Writing—review & editing: JX, YJL, RMH, JLL

Competing interests

All authors declare they have no competing interests.

Supplementary Materials for

Elevated *in-situ* Vp/Vs preceding hydraulic-fracturing-induced earthquakes

Jian Xu[1,2*], Yajing Liu[1*], Junlun Li[2,4,5*], Marco P. Roth[3], Rebecca M. Harrington[3], Yicheng He[6]

[1]Department of Earth and Planetary Sciences, McGill University, Montreal, Quebec, Canada.
[2]State Key Laboratory of Precision Geodesy, School of Earth and Space Sciences, University of Science and Technology of China, Hefei 230026, China.
[3]Institute of Geosciences, Ruhr University Bochum, Bochum, Germany.
[4]Mengcheng National Geophysical Observatory, University of Science and Technology of China, Hefei, Anhui, China.
[5]Anhui Provincial Key Laboratory of Subsurface Exploration and Earthquake Hazard Prevention, Hefei, 230031, China
[6]Jiangsu Earthquake Agency, Nanjing, China.

Corresponding authors: Jian Xu (jian.xu2@mail.mcgill.ca)
Yajing Liu (yajing.liu@mcgill.ca)
Junlun Li (lijunlun@ustc.edu.cn)

This PDF file includes:

Supplementary Text 1
Supplementary Figs. 1 to 21
Supplementary Movies 1 to 2

Supplementary Text

Supplementary Text 1: Travel-Time vs. Arrival-Time

Here we prove that the method used in this study equals to that in Lin et al. (25). For each event, we have:

$$t_{arrival} = t_{event}(true) + t_{travel}(true) = t_{event}(obs) + t_{travel}(obs), \quad (1)$$

where $t_{arrival}$ is arrival time, t_{event} is event origin time, and t_{travel} is travel time. "true" and "obs" indicate the true time and observed time, respectively. The observed origin time contains measurement error, that is:

$$t_{event}(obs) = t_{event}(true) + Et_{event}, \quad (2)$$

where Et_{event} is the error of event origin time. Combining (1) and (2), we have

$$t_{arrrival} = t_{event}(true) + t_{travel}(obs) + Et_{event}, \quad (3)$$

that is:

$$t_{travel}(obs) = t_{arrrival} - t_{event}(true) - Et_{event}. \quad (4)$$

Supposing we have two events 1 and 2, we have:

$$t1_{travel}(obs) = t1_{arrrival} - t1_{event}(true) - Et1_{event} \quad (5)$$

$$t2_{travel}(obs) = t2_{arrrival} - t2_{event}(true) - Et2_{event}. \quad (6)$$

The differential travel time between these two events is:

$$\Delta t_{travel}(obs) = \Delta t_{arrrival} - \Delta t_{event}(true) - \Delta Et_{event} \quad (7)$$

where:

$$\Delta t_{travel}(obs) = t2_{travel}(obs) - t1_{travel}(obs) \quad (8)$$

$$\Delta t_{arrrival} = t2_{arrival} - t1_{arrival} \quad (9)$$

$$\Delta t_{event}(true) = t2_{event}(true) - t1_{event}(true) \quad (10)$$

$$\Delta Et_{event} = Et2_{event} - Et1_{event}. \quad (11)$$

Supposing we have stations from 1 to n for each event, we have:

$$\Delta t_{travel,st1}(obs) = \Delta t_{arrrival,st1} - \Delta t_{event}(true) - \Delta Et_{event} \quad (12)$$

$$\Delta t_{travel,st2}(obs) = \Delta t_{arrrival,st2} - \Delta t_{event}(true) - \Delta Et_{event} \quad (13)$$

…

$$\Delta t_{travel,stn}(obs) = \Delta t_{arrrival,stn} - \Delta t_{event}(true) - \Delta Et_{event}, \quad (14)$$

where $\Delta t_{event}(true)$ and ΔEt_{event} are constants for each event. The mean of the differential travel times is:

$$mean\big(\Delta t_{travel}(obs)\big) = mean(\Delta t_{arrrival}) - \Delta t_{event}(true) - \Delta Et_{event}. \quad (15)$$

Subtracting (15) from (12)-(14), we have:

$$\Delta t_{travel,st1}(obs) - mean\big(\Delta t_{travel}(obs)\big) = \Delta t_{arrrival,st1} - mean(\Delta t_{arrrival}) \quad (16)$$

$$\Delta t_{travel,st2}(obs) - mean\big(\Delta t_{travel}(obs)\big) = \Delta t_{arrrival,st2} - mean(\Delta t_{arrrival}) \quad (17)$$

…

$$\Delta t_{travel,stn}(obs) - mean\big(\Delta t_{travel}(obs)\big) = \Delta t_{arrrival,stn} - mean(\Delta t_{arrrival}), \quad (18)$$

where $\Delta t_{stn} - mean(\Delta t_{travel}(obs))$ is the measurements used for fitting in our study, and $\Delta t_{arrrival,stn} - mean(\Delta t_{arrrival})$ is that used in Lin and Shearer (2007), which is equal to each other.

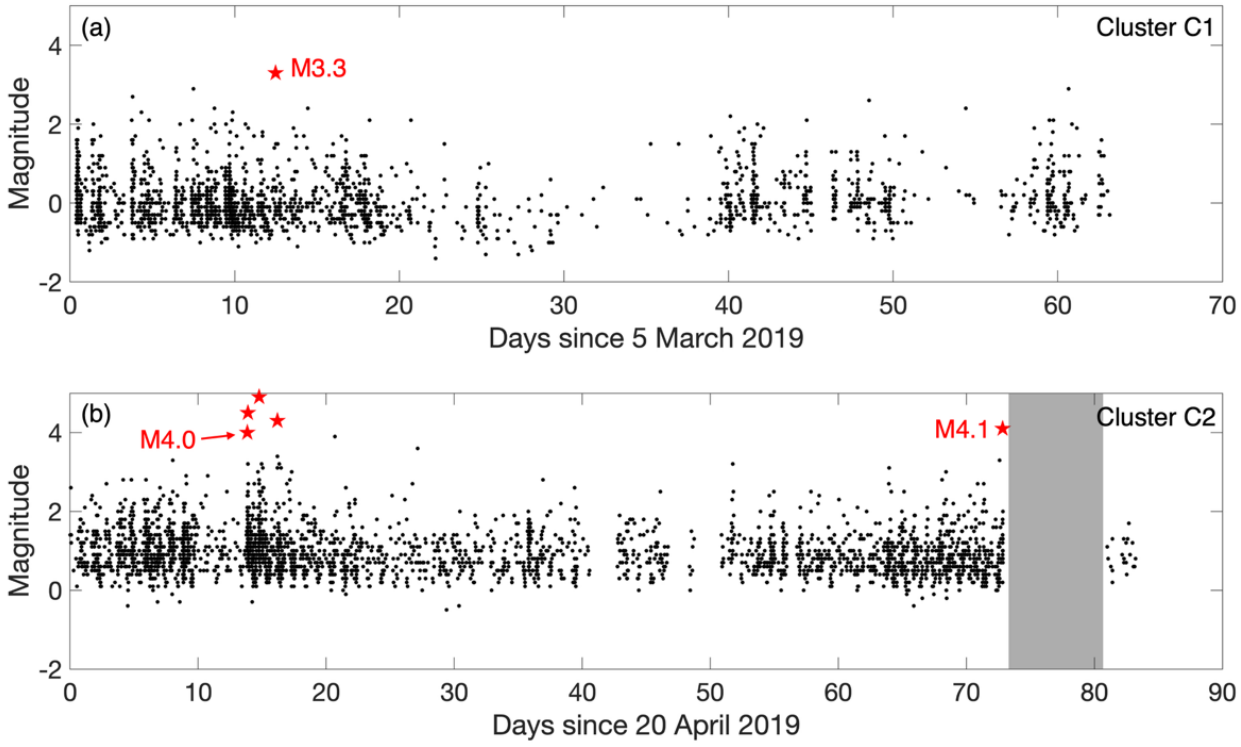

Supplementary Fig. 1.

Magnitude-time distribution of clusters C1 (a) and C2 (b). The magnitudes of completeness of clusters C1 and C2 are $M_c - 0.3$ and $M_c 0.6$, respectively. The gray shaded panel in (b) indicates a period of data loss likely due to damages to local telecommunication infrastructures between July 2 and July 8, 2023.

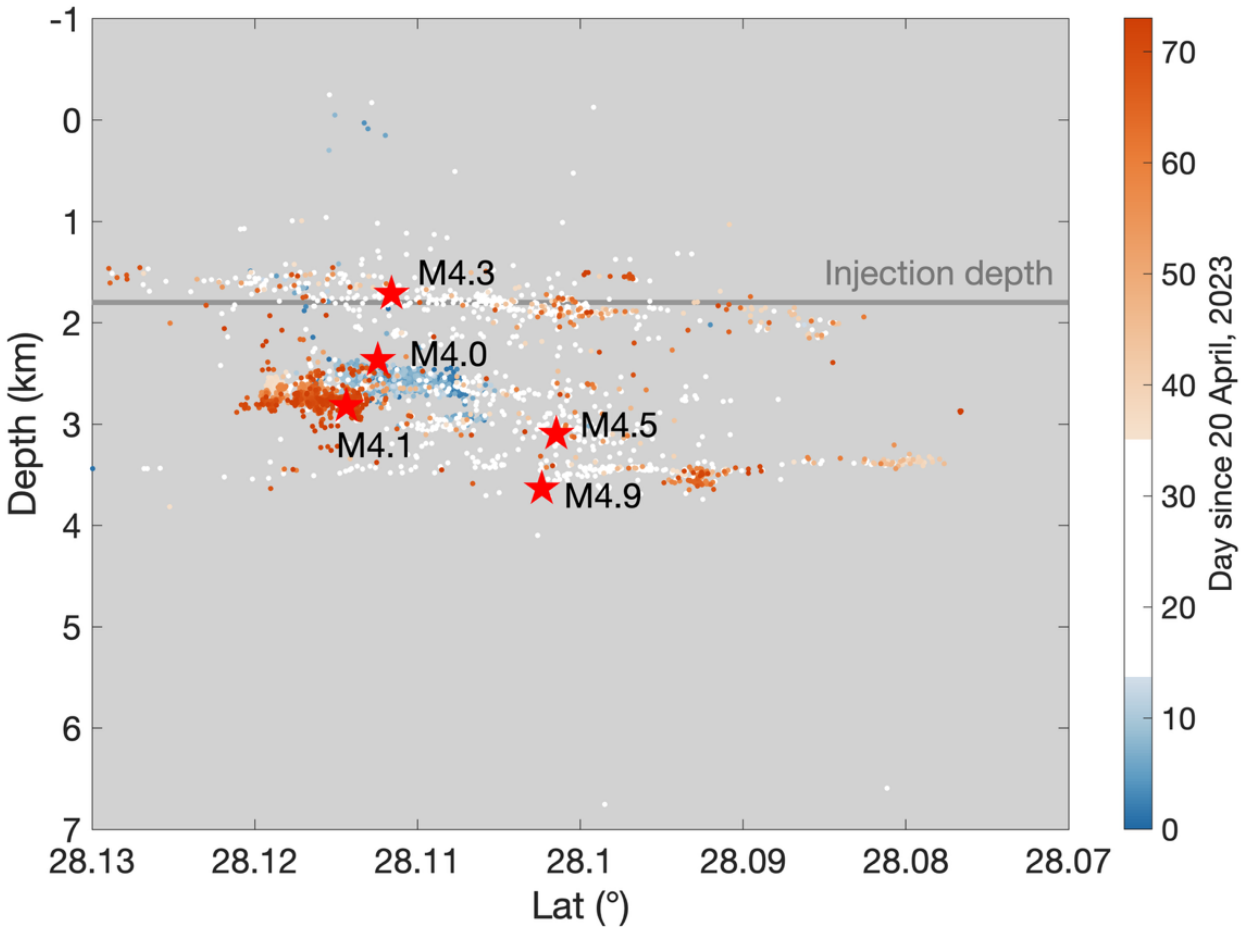

Supplementary Fig. 2.

Seismicity in cluster C2 projected in the depth-latitude plane.

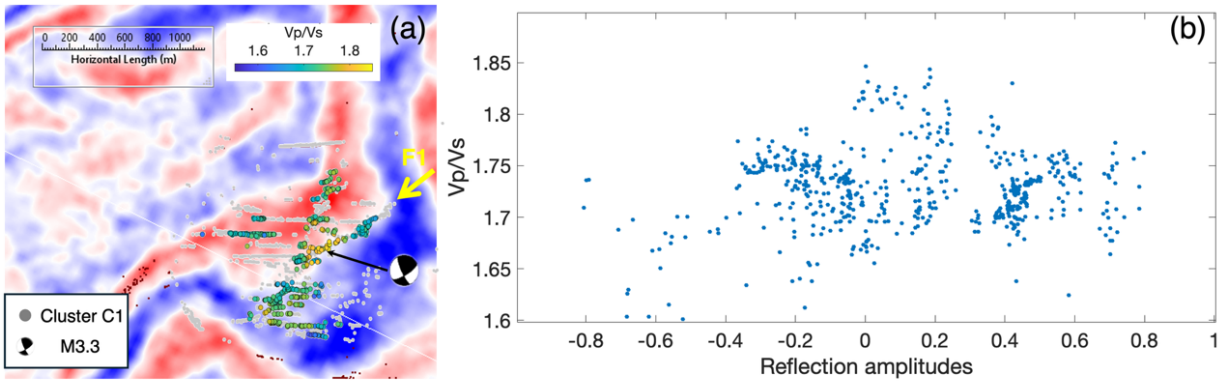

Supplementary Fig. 3.

Vp/Vs values compared to seismic reflection amplitudes for cluster C1. (a) Horizontal active-source reflection profile at the hypocentral depth of the M3.3 event. Red-blue background color indicates rescaled reflection amplitudes. The dots are earthquakes color-coded by Vp/Vs values. (b) Vp/Vs values versus reflection amplitudes.

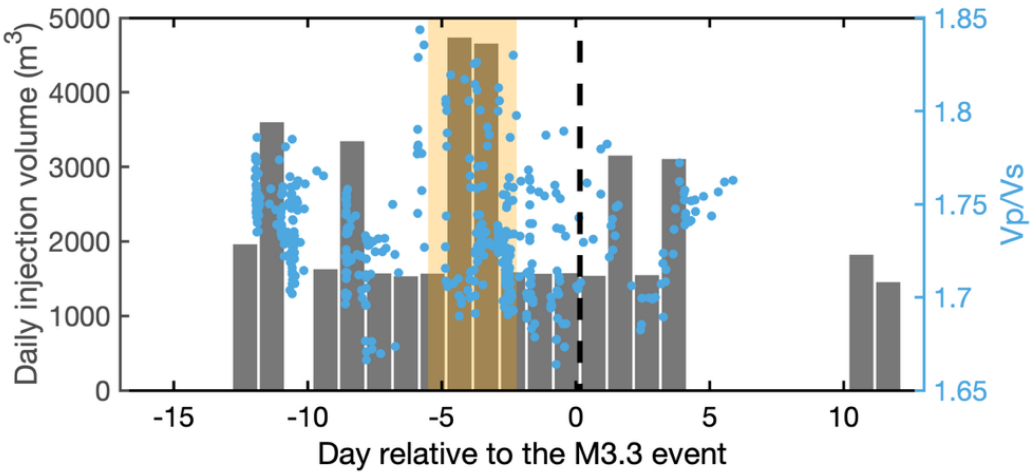

Supplementary Fig. 4.

Time correlation between elevated Vp/Vs values (>1.8) and large injection volume (>4000 m^3) highlighted by yellow shaded zone. The gray bars denote the daily injection volume. The black line is the origin time of M3.3 event.

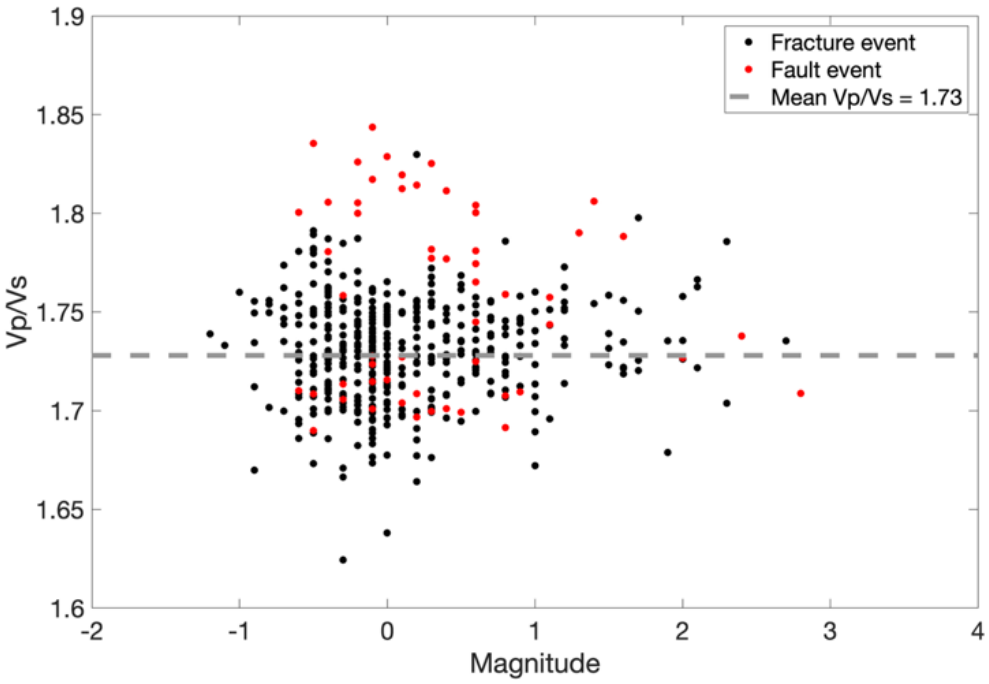

Supplementary Fig. 5.

Vp/Vs values versus magnitudes. Black and red dots represent seismicity inside and outside the fault F1 zone defined in Fig. 3B. The gray dashed line denotes the average Vp/Vs value of 1.73.

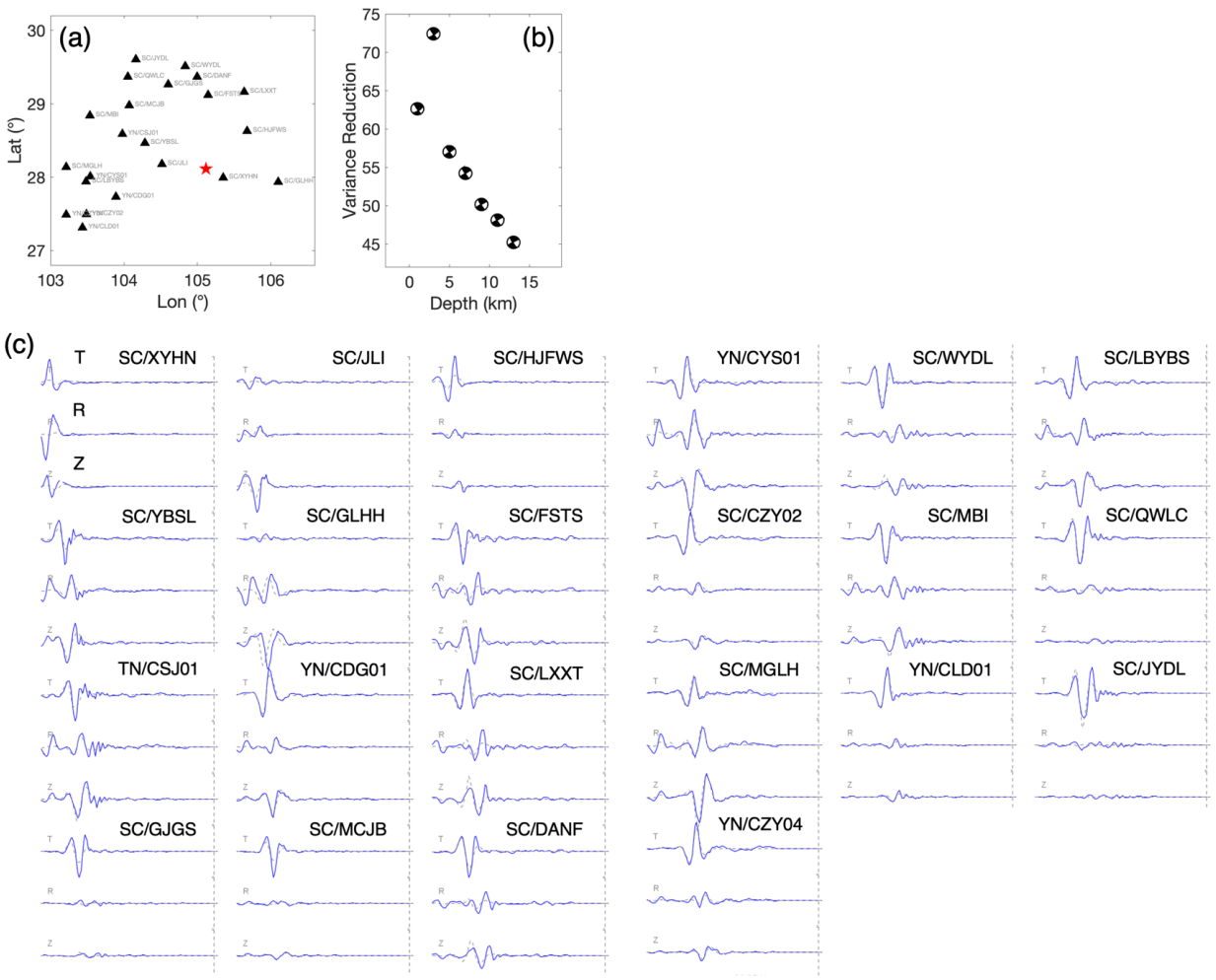

Supplementary Fig. 6.

Focal mechanism solution for the M4.1 event in cluster C2. (a) Distribution of earthquake epicenters (red star) and seismic stations (black triangles) within 200 km. (b) Variance reduction along depths. The best fit is located at the depth of 3 km. (c) The waveform fitting at tangential (T), radial (R) and vertical (Z) components. Blue solid and grey dashed lines represent the observed and synthetic waveforms, respectively. Station names are labelled at the upper right of each station panel.

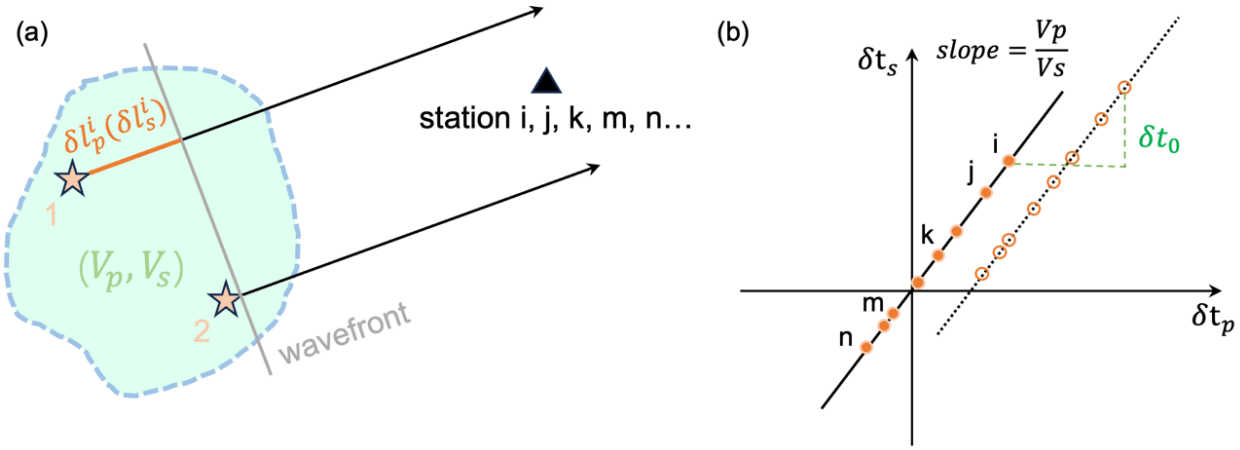

1041

1042 **Supplementary Fig. 7.**

1043 Schematic illustration of the fundamental principle of the *in-situ* Vp/Vs analysis
1044 method, modified from Lin and Shearer[25].

1045

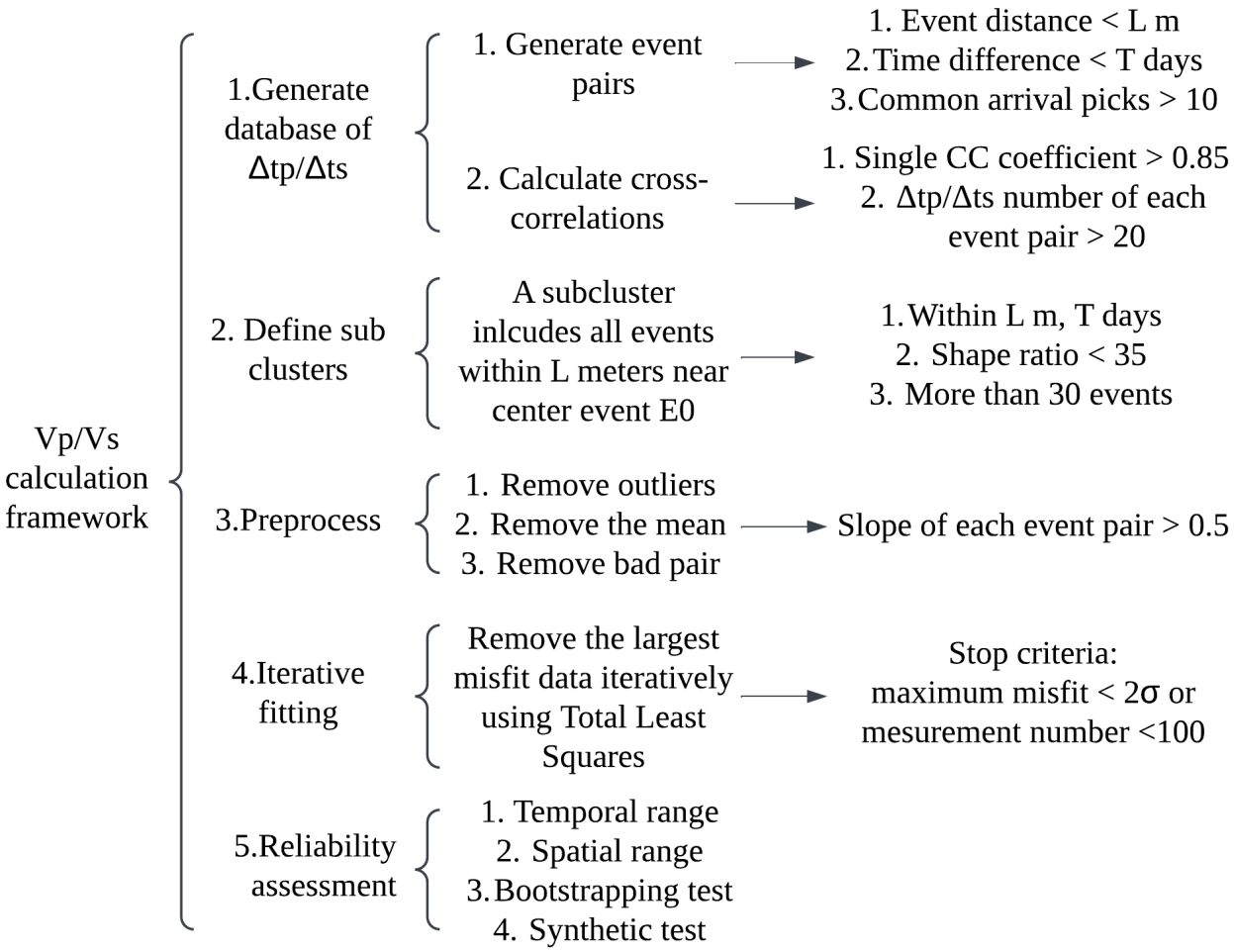

Supplementary Fig. 8.

Workflow of Vp/Vs analysis. “T” and “L” represent the time window and radius, respectively.

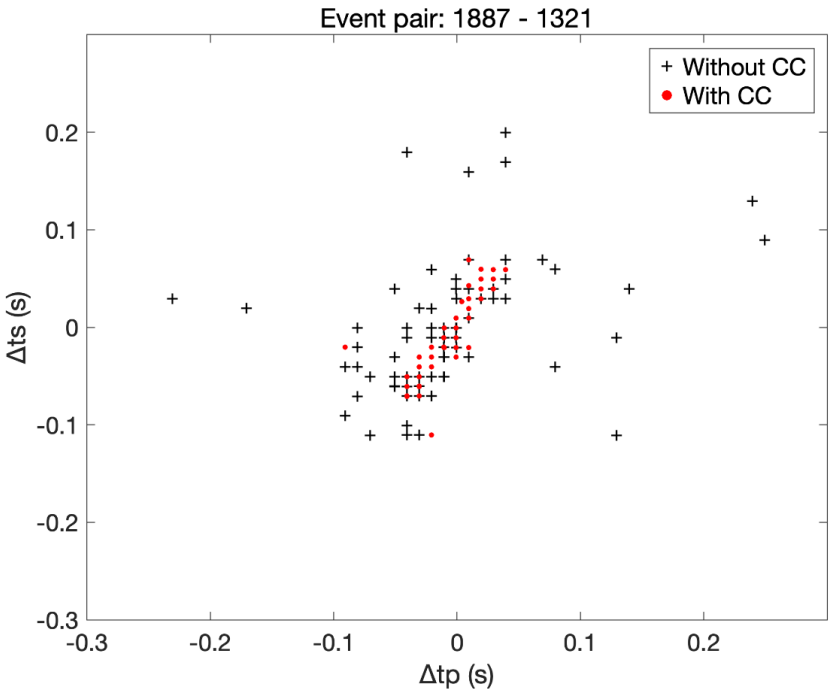

Supplementary Fig. 9.

Cross-correlation (CC) improves the travel-time-difference measurements for an event pair.

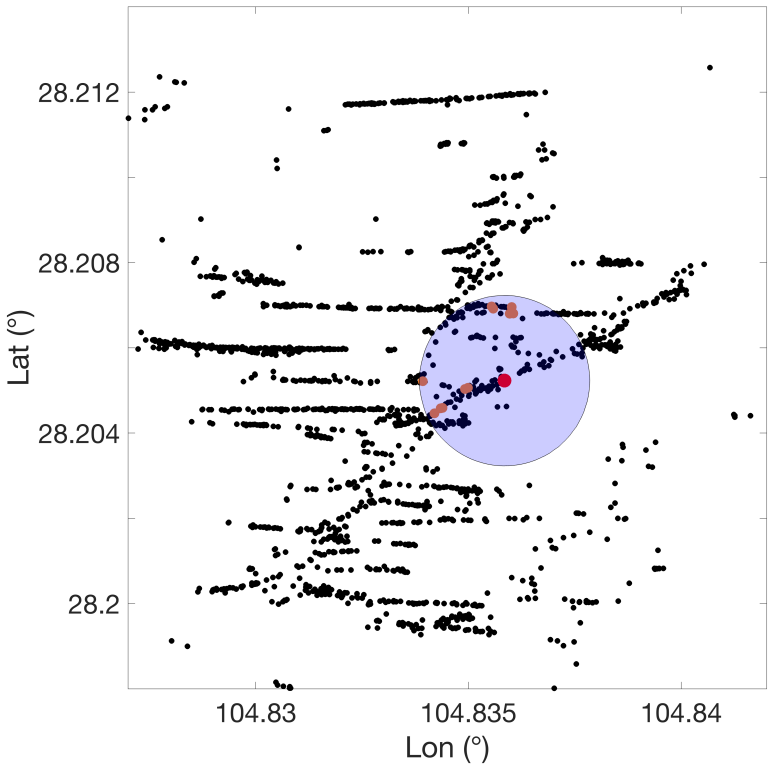

Supplementary Fig. 10.

Schematic illustration for the definition of a sub-cluster. Black dots represent all events in cluster C1. Red dots indicate the target event of a sub-cluster, and brown dots denote the events included in the sub-cluster after applying the spatiotemporal window.

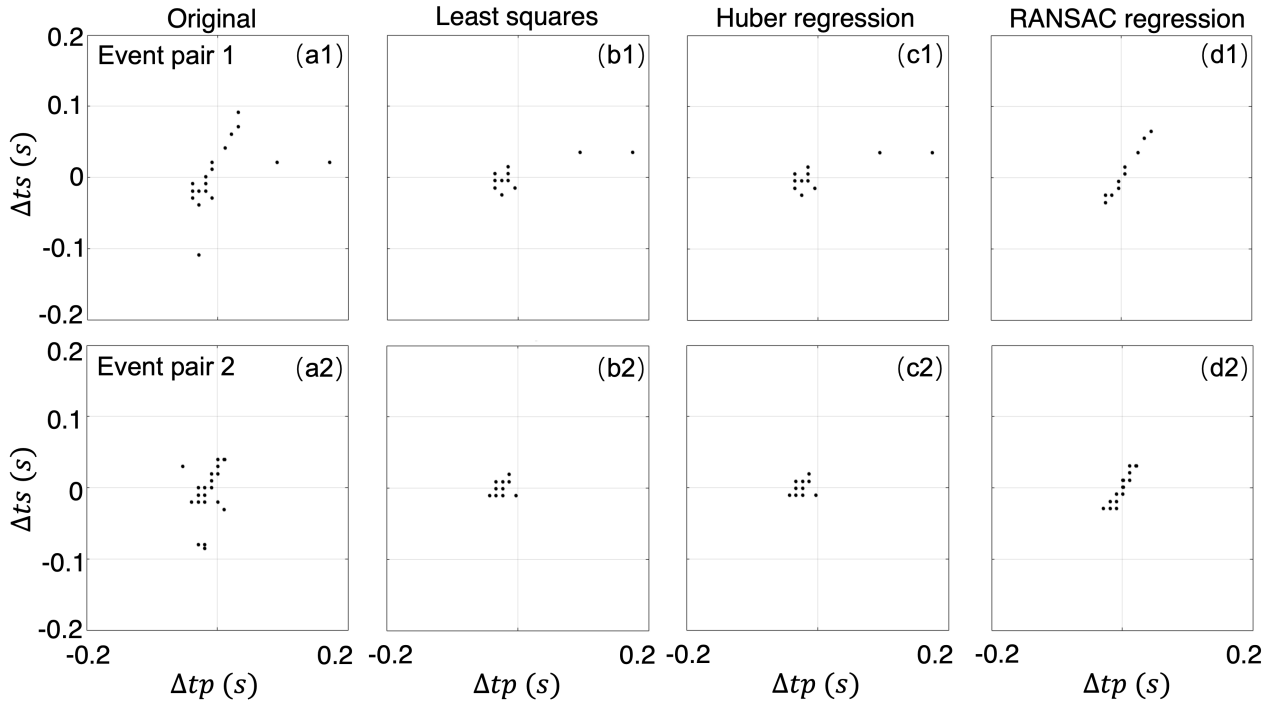

Supplementary Fig. 11.

Two examples of event-pair preprocessed results using different methods. “Original” denotes the raw, unprocessed differential travel times, while “Least squares,” “Huber regression,” and “RANSAC regression” represent the results after outlier removal and mean subtraction using conventional least-squares fitting, the L1–L2 hybrid norm, and random sample consensus (RANSAC), respectively.

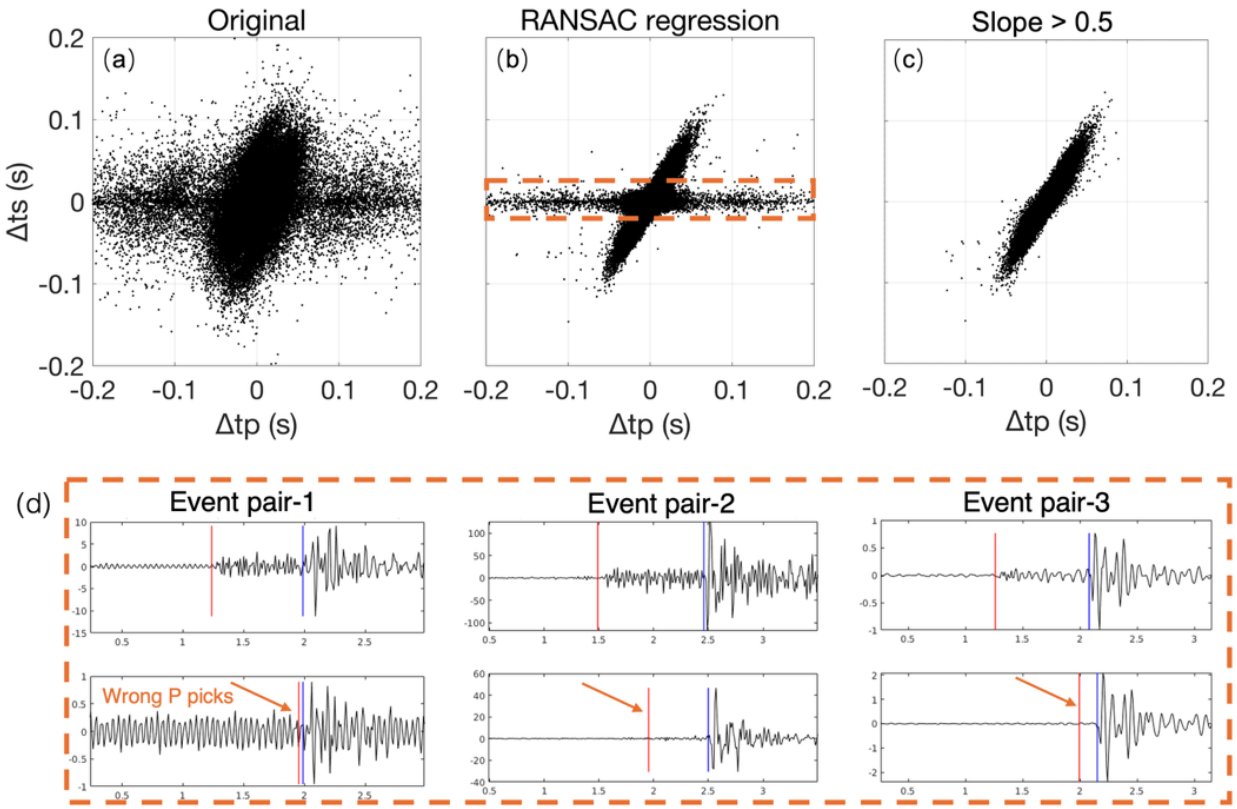

Supplementary Fig. 12.

An example of preprocessed results for a sub-cluster using the RANSAC method. (a) Unprocessed differential travel times of all event pairs within the sub-cluster. (b) Differential travel times after removing outliers using the random sample consensus (RANSAC) method. (c) Final measurements after applying an additional selection criterion (slope >0.5) for each event pair to remove anomalous values concentrated around Δts = 0 s due to incorrect P-wave phase picking of noisy waveform. (d) Three event-pair examples for incorrect P-wave picks.

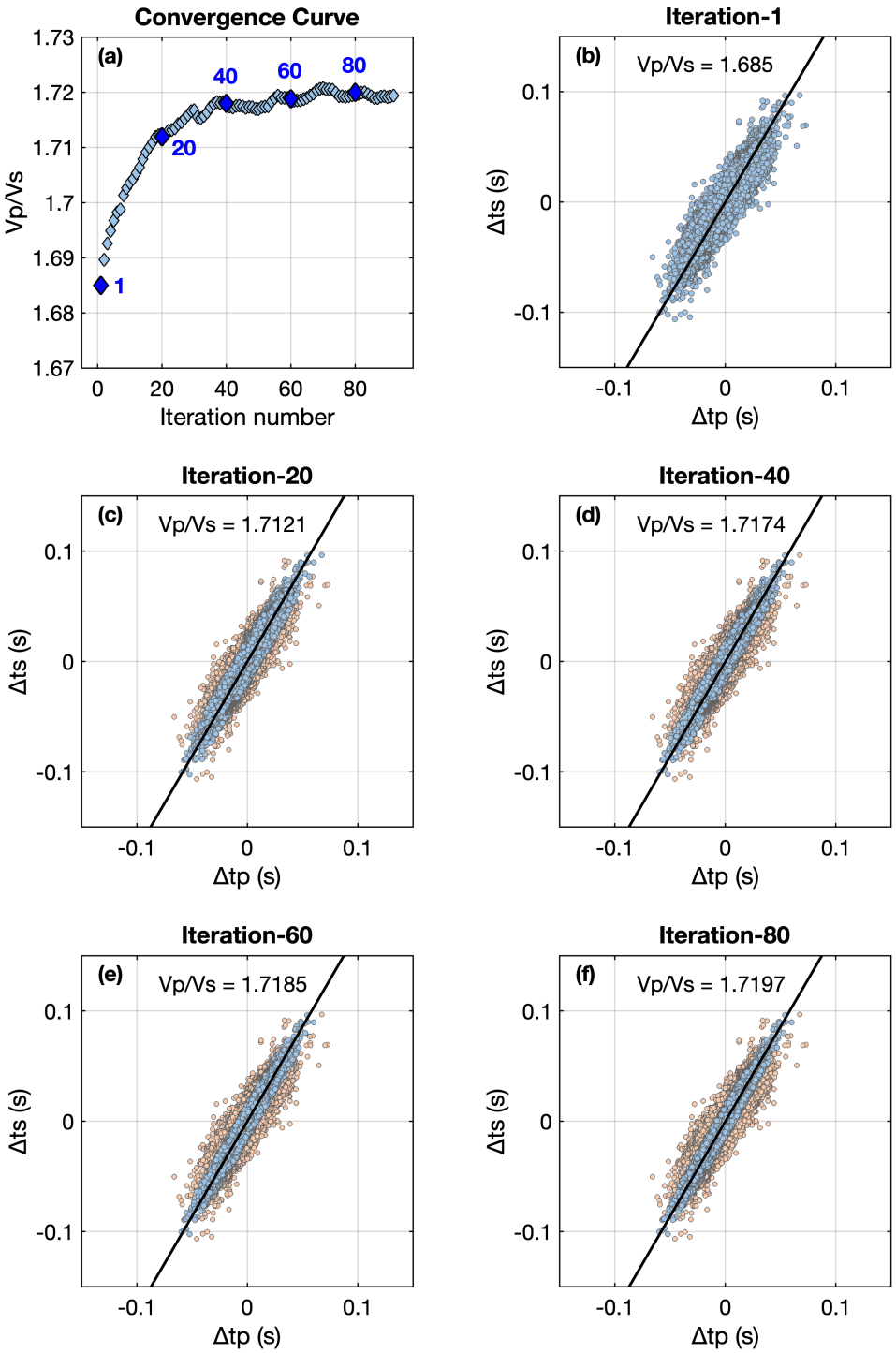

Supplementary Fig. 13.

Iterative fitting procedure for Vp/Vs. (a) Evolution of Vp/Vs with iteration; dark blue squares mark the iterations whose fitting results are shown in panels (b–f). (b–f) Results of the 1st, 20th, 40th, 60th, and 80th iterations. Light blue circles indicate the differential travel-time data retained in each iteration, and orange circles indicate the data removed.

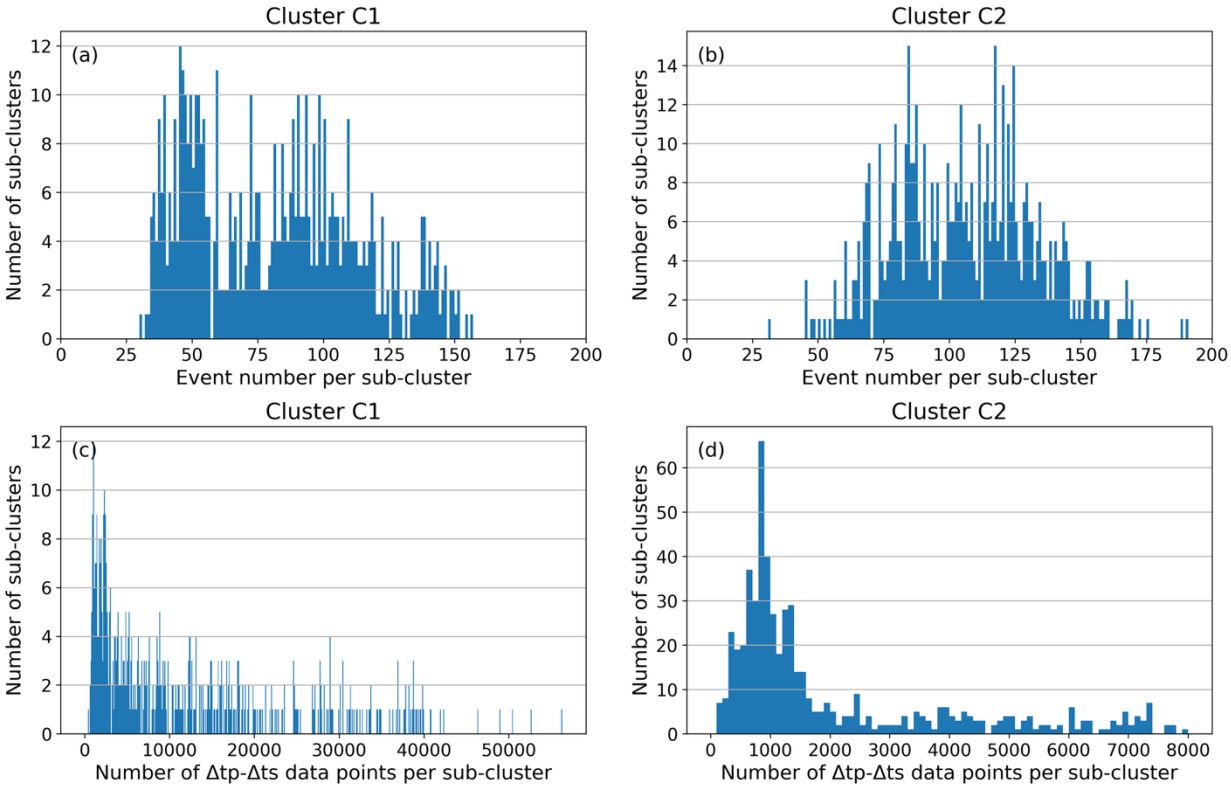

1087

1088 **Supplementary Fig. 14.**

1089 Statistics on number of events and differential travel-time data points in each sub-
1090 cluster for cluster C1 (a, c) and cluster C2 (b, d), respectively.

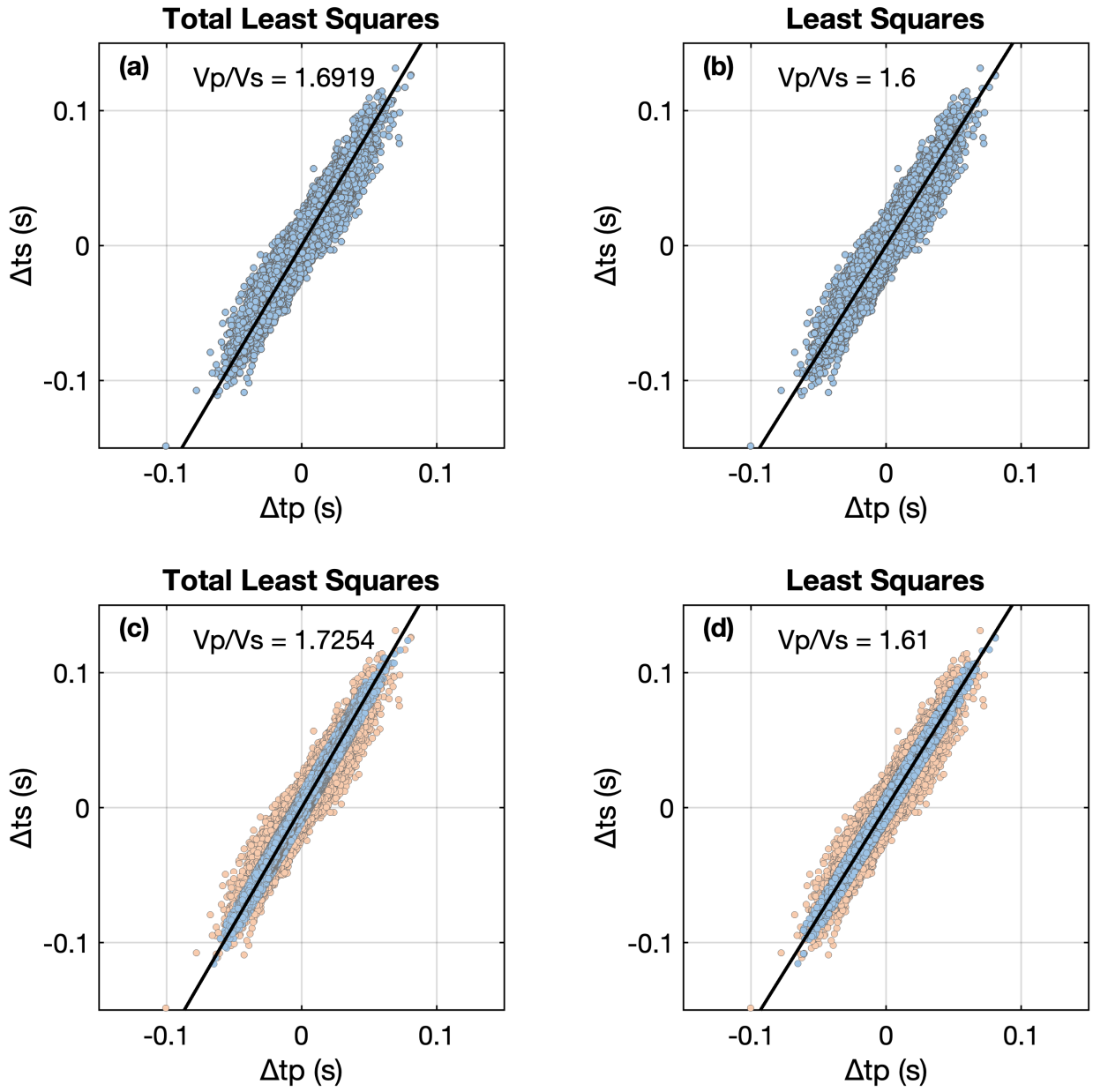

Supplementary Fig. 15.

Fitting method comparison. (a) Total least-squares fit using all data. (b) Conventional least-squares fit using all data. (c) Total least-squares result after iterative fitting. Blue dots indicate the data retained in the final fit, and orange dots indicate the data removed during the iterations. (d) Least-squares result after iterative fitting.

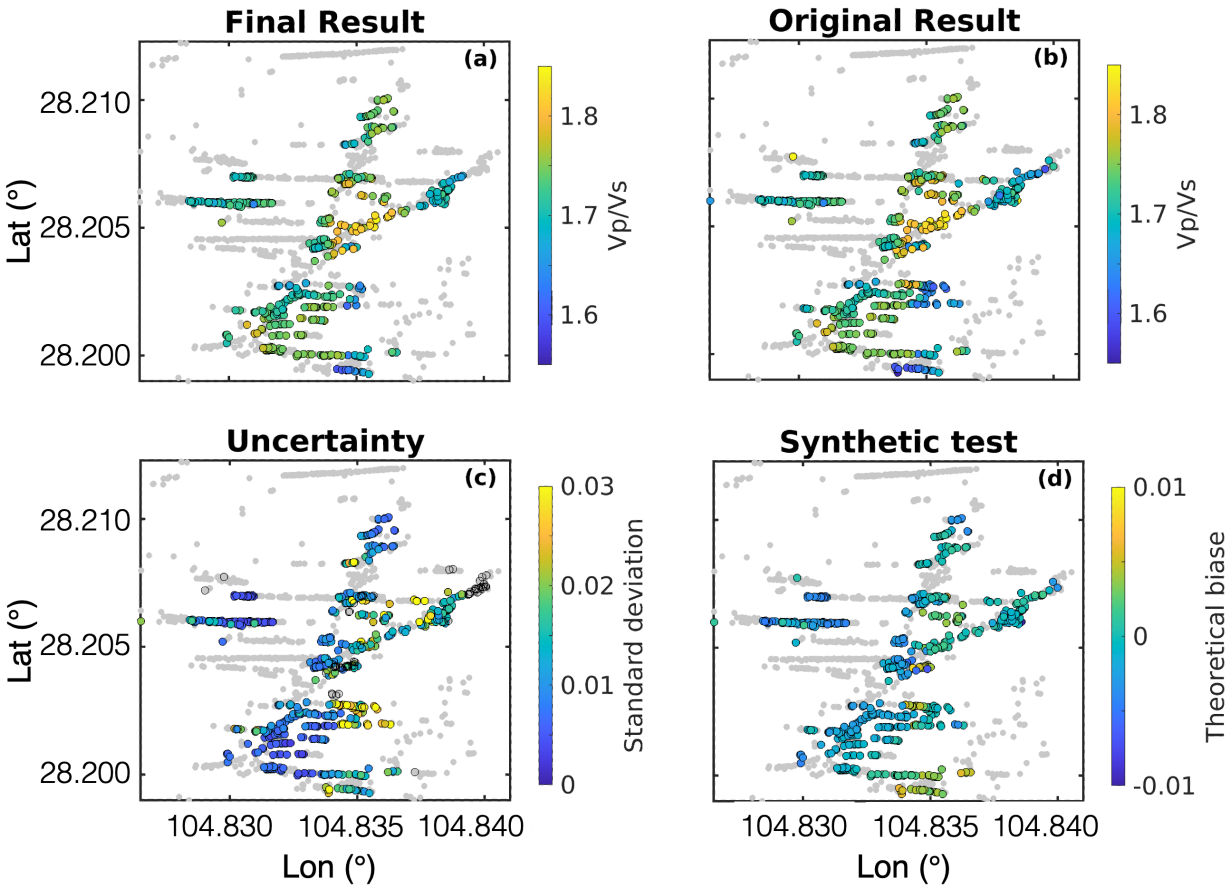

1098

1099 **Supplementary Fig. 16.**

1100 Uncertainty and synthetic tests for cluster C1. (a) Final results retained after applying
1101 both the uncertainty test and the synthetic test. (b) Original results before testing; gray
1102 dots indicate event clusters that do not satisfy the criteria on event number or spatial
1103 distribution. (c) Events are color-coded by uncertainties. (d) Events are color-coded
1104 by theoretical biases.

1105

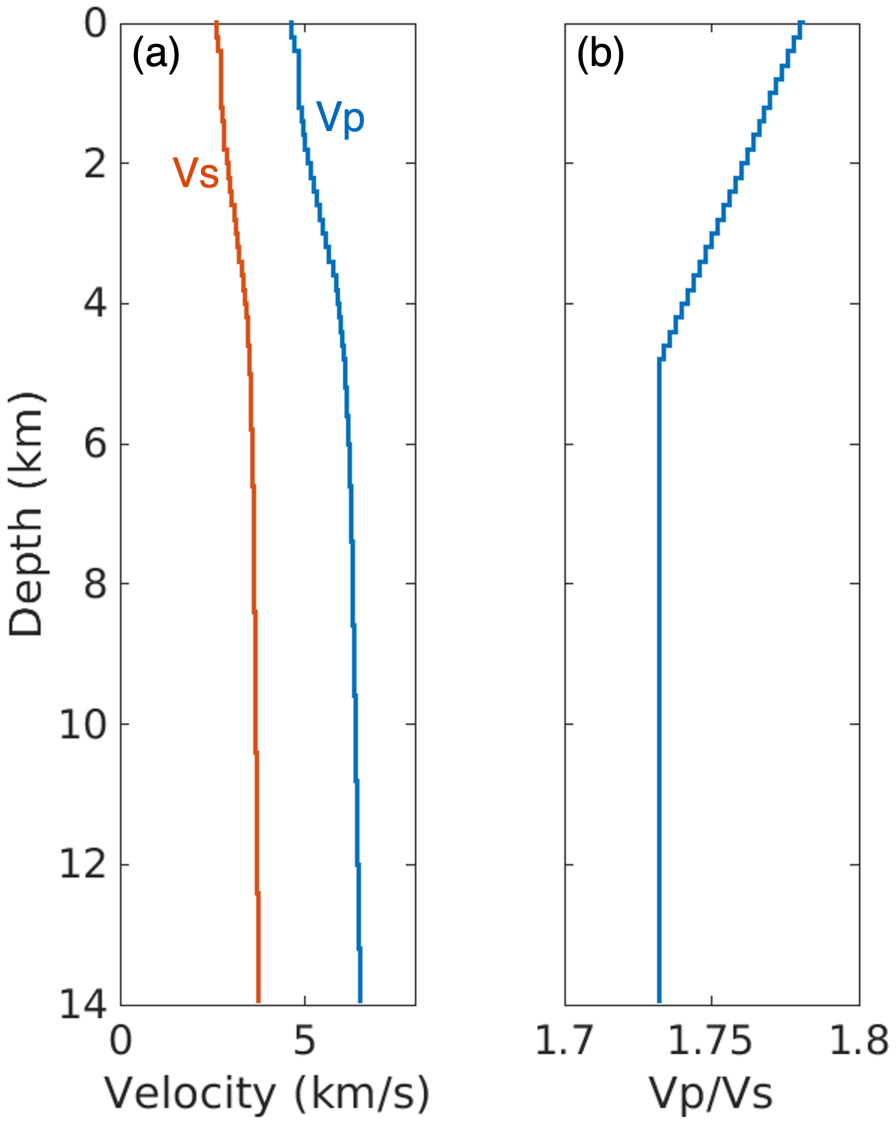

Supplementary Fig. 17.

Initial velocity models (Vp, Vs and Vp/Vs) used for the synthetic tests.

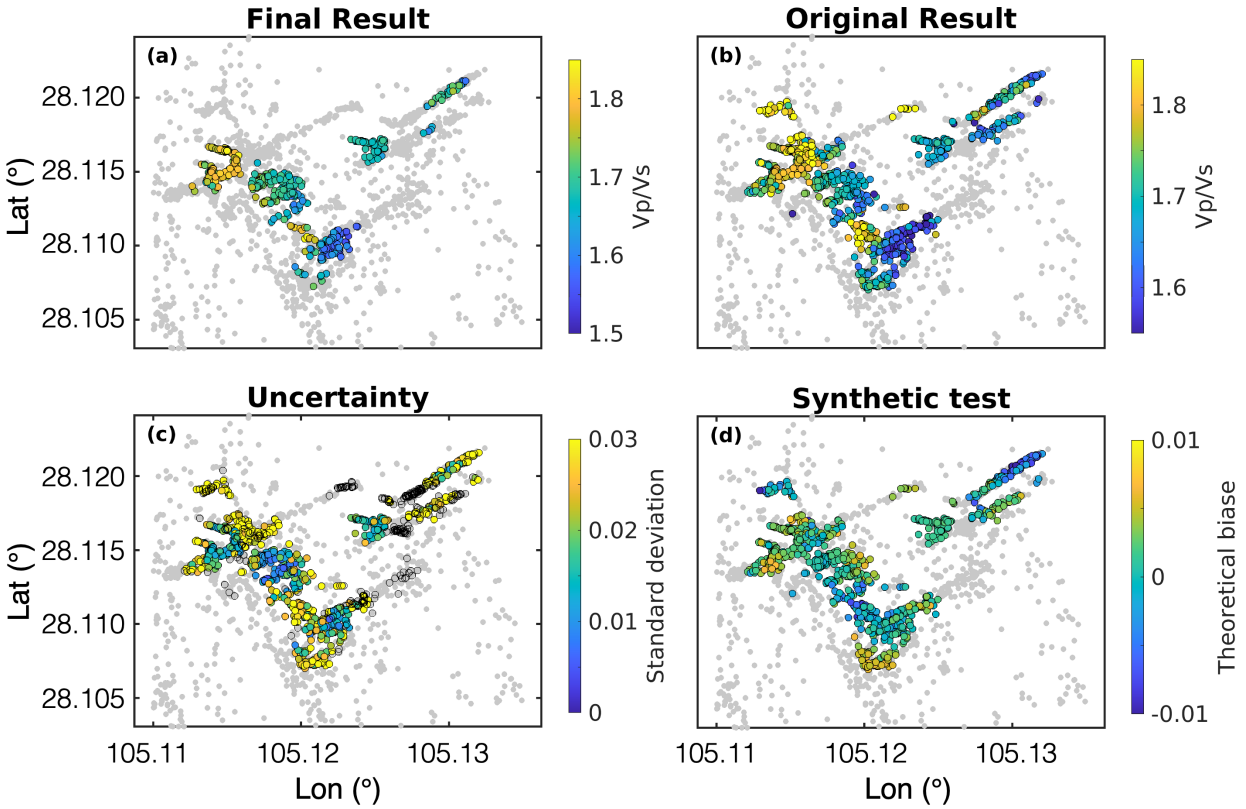

1110

1111 **Supplementary Fig. 18.**

1112 Uncertainty and synthetic tests for cluster C2. (a) Final results retained after applying
1113 both the uncertainty test and the synthetic test. (b) Original results before testing; gray
1114 dots indicate event clusters that do not satisfy the criteria on event number or spatial
1115 distribution. (c) Events are color-coded by uncertainties. (d) Events are color-coded
1116 by theoretical biases.

1117

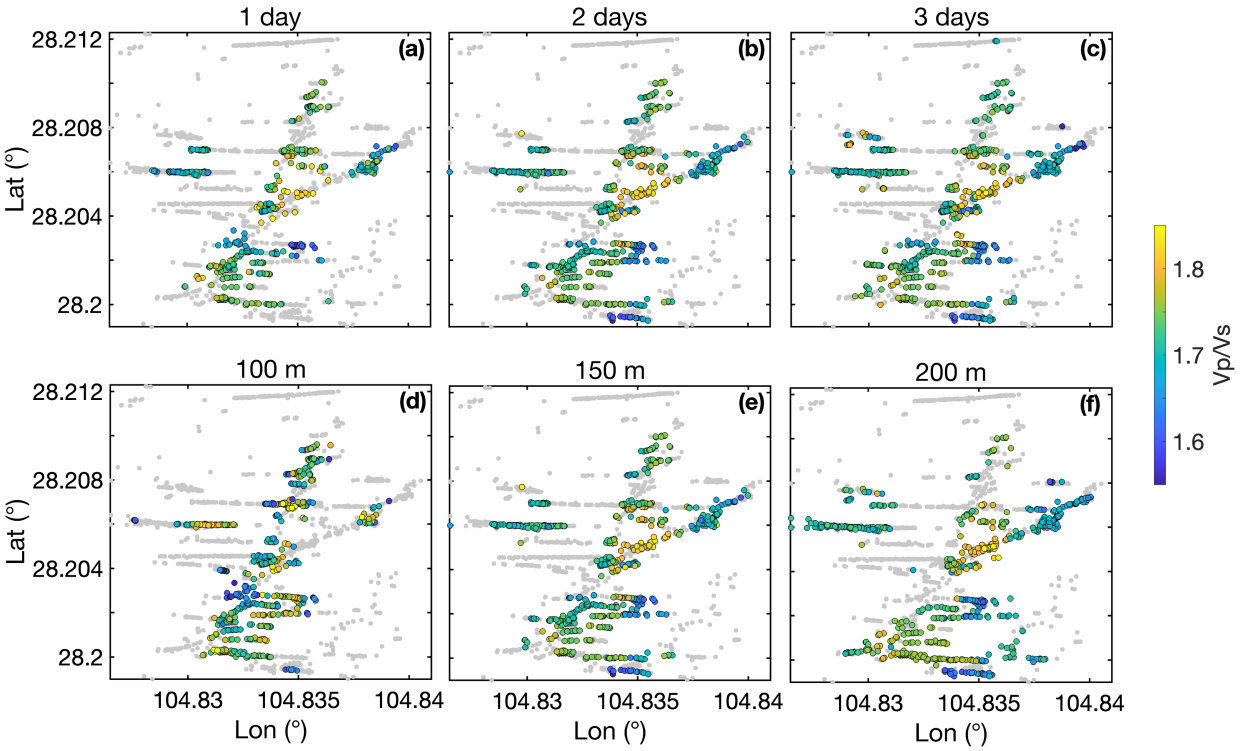

Supplementary Fig. 19.

Fitting results for cluster C1 using different spatial-temporal windows. Panels (a–c) test different temporal windows with the spatial range fixed at 150 m, whereas panels (d–f) test different spatial ranges with the temporal window fixed at 2 days.

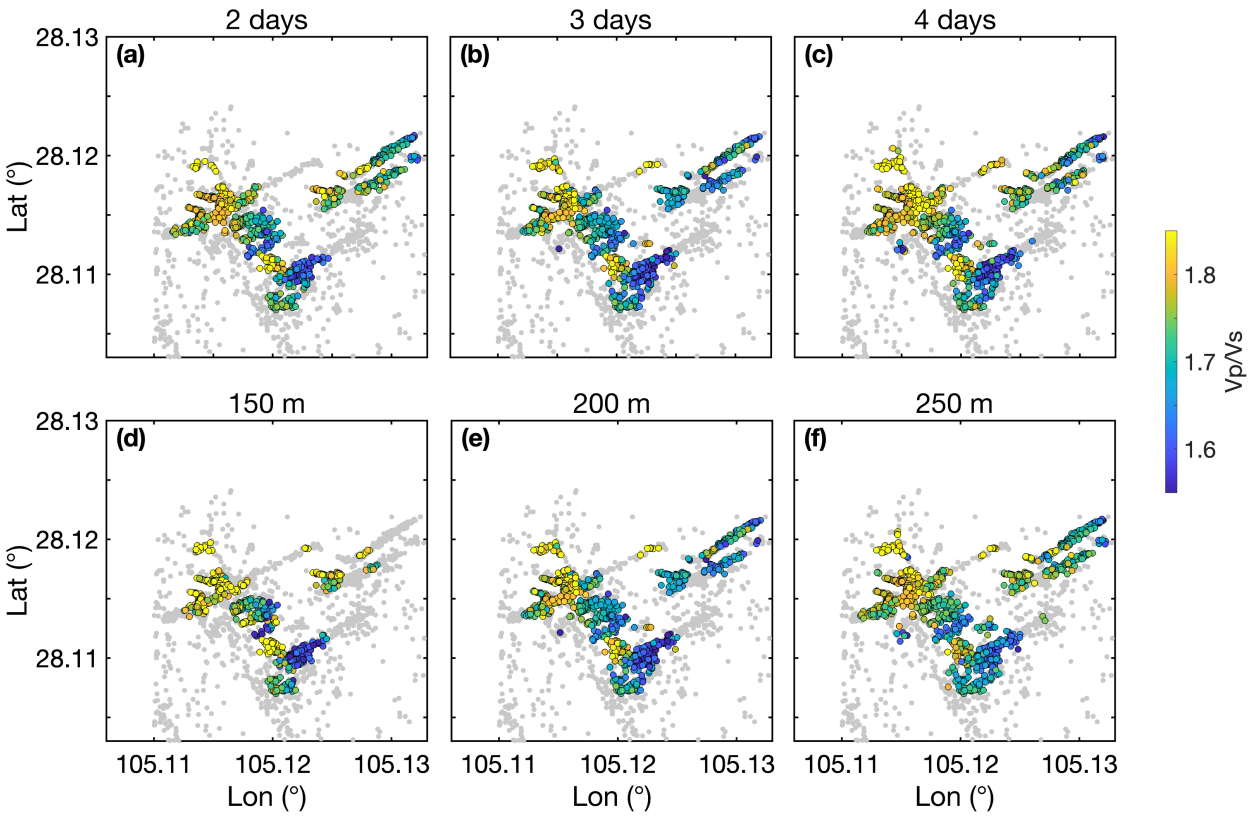

Supplementary Fig. 20.

Fitting results for cluster C2 using different spatial–temporal windows. Panels (a–c) test different temporal windows with the spatial range fixed at 200 m, whereas panels (d–f) test different spatial ranges with the temporal window fixed at 3 days.

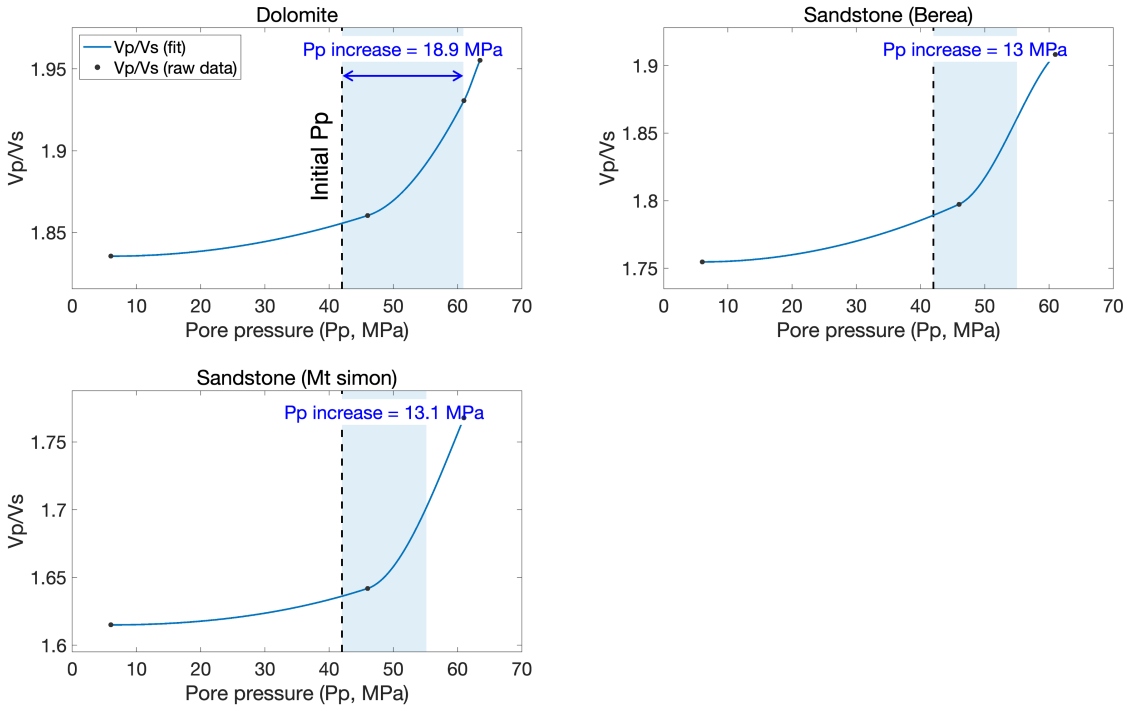

Supplementary Fig. 21.

Vp/Vs measurements of different rock samples. The raw data points of pore pressure and Vp/Vs values are extracted from Christensen[44] with a confining stress of ~66 MPa. We fit the measured Vp/Vs as functions of pore pressure using a shape-preserving piecewise cubic Hermite interpolating polynomial (PCHIP). The light blue regions highlight the estimated pore-pressure increase from initial ~42 MPa given a 4% increase of Vp/Vs.

Supplementary Movie 1.

Spatiotemporal evolution of seismicity in cluster C1.

Supplementary Movie 2.

Spatiotemporal evolution of seismicity in cluster C2.